



**Design Optimisation of Metal Hydride Hydrogen
Storage Systems by Computational Fluid Dynamics
and Machine Learning**

Siwoo Jung

A thesis in fulfilment of the requirements for the degree of
Master of Philosophy

School of Chemical Engineering

Faculty of Engineering

August 2024

Disclaimer

The current version of thesis is neither a final nor an official document. This is a draft which is awaiting the supervisor's final approval and will be officially submitted to the University of New South Wales by 8th of September 2024. This is a draft to provide a reference to recruiters.

Abstract

As net-zero emissions have never been more crucial globally, the importance of hydrogen has also risen. In terms of hydrogen storage, metal hydride hydrogen storage systems (MHHSS) are promising due to moderate operating temperatures and pressures and higher storage density. However, they still have a few drawbacks, such as heavy weight, slower reaction rates, and the necessity of efficient thermal management. Therefore, this thesis addresses the design optimisation of MHHSS using computational fluid dynamics (CFD) to improve reaction rates and thermal management. Additionally, the performance of MHHSS can be predicted with a powerful computational tool, machine learning (ML). As ML-integrated CFD research on MHHSS has not yet been widely studied, this thesis addresses ML analysis to predict hydrogen reaction time given varying design parameters.

The first study focuses on optimising a metal hydride (MH) hydrogen storage reactor's reaction rates and thermal management using phase-change material (PCM) and embedded copper fins. The results demonstrate that the MH-Fin-PCM hydrogen storage reactor can significantly improve the hydrogen absorption and desorption reactions, with reversibility rates of 94.9% and 92.9%, respectively. Additionally, it works as an independent system, which does not require a conventional heat transfer fluid (HTF). The second study simulates multiple MH hydrogen storage reactors with different internal coil design parameters. After collecting CFD results, various supervised ML models are developed and optimised to predict the hydrogen absorption time based on specific values of internal coil design parameters. The results show that ML can effectively predict the hydrogen absorption time, highlighting its potential application in predicting the design requirements of MHHSS in the industry. Overall, the studies in this thesis lay the groundwork for scaling up and optimising MHHSS for practical use in industry and real-life applications.

Acknowledgement

Firstly, I extend my deepest gratitude to my supervisor, Prof. Yansong Shen, for enlightening and supporting me in building my career in the hydrogen industry. Without your initial supervision during my honours degree in 2018, I would not have had an opportunity to dive into hydrogen research, followed by industry experience in the hydrogen field. In addition, I sincerely appreciate your offering me the opportunity to be in the ProMO Lab again to resume my research. Your support and guidance have led me to complete my M.Phil. candidature and will be the foundation for my future career.

I am also significantly grateful to my co-supervisor, Dr. Yuting Zhuo, who has also supported me since 2018. You have been an academic mentor and a friend in and out of UNSW. Your enthusiasm for research has motivated me during my journey to an M.Phil. degree. I hope I can also support you throughout your future career.

I express my appreciation to all ProMO Lab colleagues who work hard to achieve their goals. You are each a competitive individual full of passion and enthusiasm.

Lastly, I thank my father, Koodong Jung, and beloved mother, Soonam Choi, for caring for me and letting me be who I am today. You have always been my greatest mentor, and I will always be your proud son. I also thank my younger brother, Junyoung Jung, who has been my best friend. I hope everything goes well on your journey in Germany.

Once again, I appreciate all the individuals I have met throughout my M.Phil. candidature.

Contents

Disclaimer	I
Abstract	II
Acknowledgement.....	III
Contents	IV
Abbreviations	VII
List of Figures	VIII
List of Table	XII
List of Nomenclature.....	XIII
Chapter 1 Introduction	1
1.1. Background	1
1.2. Objective	3
1.3. Thesis Organisation.....	3
Chapter 2 Literature Review	5
2.1. Reaction Mechanisms	5
2.2. Experimental Optimisation	9
2.3. Numerical Optimisation	11
2.4. Knowledge Gaps	19
Chapter 3 Numerical evaluation of MHHSS with PCM.....	20

3.1.	Introduction.....	20
3.2.	Model Description.....	26
3.2.1.	Base case	26
3.2.2.	Design #1	29
3.2.3.	Design #2 and #3.....	29
3.3.	Numerical Setting.....	31
3.3.1.	Governing equations for the MH bed	31
3.3.2.	Governing equations for the PCM bed	31
3.3.3.	Initial and boundary conditions.....	33
3.4.	Results and Discussion.....	34
3.4.1.	Basic MH-PCM reactor (Base Case)	34
3.4.2.	Optimised designs (Design #1 ~ #3).....	38
3.4.3.	Reversibility test for Design #3	44
3.5.	Summary	54
Chapter 4	MHHSS design optimisation by the integration of CFD and ML.....	57
4.1.	Introduction.....	57
4.2.	Method	59
4.2.1.	Numerical model.....	60
4.2.2.	Machine learning analysis.....	63
4.3.	Results and Discussion.....	66
4.3.1.	Effects of coil design parameters	66

4.3.2. Machine learning analysis.....	70
4.4. Summary	73
Chapter 5 Conclusion and Future Perspectives.....	75
REFERENCES.....	77

Abbreviations

ABS	Absorption
ANN	Artificial Neural Network
CFD	Computational Fluid Dynamics
DES	Desorption
DTR	Decision Tree Regression
FEA	Finite Element Analysis
FEM	Finite Element Method
HTF	Heat Transfer Fluid
H/M	Hydrogen to metal atomic ratio
LaNi ₅	Lanthanum Nickel
LASSO	Least Absolute Shrinkage and Selection Operator
LiNO ₃ ·3H ₂ O	Lithium Nitrate Trihydrate
MAE	Mean Absolute Error
MAPE	Mean Absolute Percentage Error
MH	Metal Hydride
MHHSS	Metal Hydride Hydrogen Storage System
OLS	Ordinary Least Square
PCM	Phase-Change-Material
SVR	Support Vector Regression

List of Figures

Figure 1.1 Visualisation of a typical CFD process	2
Figure 1.2 Overall thesis organisation	4
Figure 2.1 PCT curve of a typical MH	7
Figure 2.2 An early design of MHHSS including cylindrical reactors and surrounding jackets studied by Ram Gopal and Srinivasa Murthy [18]	10
Figure 2.3 Experimental measurements of temperature at three different locations by Jemni et al. [13]	10
Figure 2.4 MHHSS with internal heat pipes studied by Kumar et al. [21] (a), Anbarasu et al. [24] (b), and Meng et al. [23] (c)	11
Figure 2.5 MHHSS with 9 internal straight heat transfer pipes with different distribution configurations studied by Krokos et al. [30]	12
Figure 2.6 MHHSS with the internal straight pipe (a) and the helical coil (b) studied by Wu et al. [43] Different coil parameters studied by Wang et al. [45] (c) Various complex designs of internal heat pipes studied by Wang et al. [46] (d)	13
Figure 2.7 MHHSS without any design improvement (a), with external circular fins (b), with an internal heat transfer pipe (c), and with an internal heat transfer pipe and internal embedded fins [47, 54]	14
Figure 2.8 Four different designs of internal heat transfer systems of MHHST studied by Mellouli et al. [39]	15
Figure 2.9 Three different designs of fins (a) and their effects on the hydrogen absorption time (b) studied by Bai et al. [50]	16
Figure 2.10 Complex geometries of fins [53, 58–61]	17
Figure 2.11 A study of the effect of aluminium foam on the hydrogen desorption rate conducted by Zhuo et al. [17]	18

Figure 3.1 Illustration of heat transfer between MH and PCM beds during hydrogen sorption reactions	20
Figure 3.2 Mass and volume of PCMs and the MH bed studied by Mellouli et al. [70]	22
Figure 3.3 MHHSS with PCMs and embedded fins studied by Nyamsi et al. (a) and Yao et al. (b) [78, 80]	23
Figure 3.4 Sandwich configuration of MH and PCM beds studied by Alqahtani et al. (a) and Hassan et al. (b) [82, 84]	24
Figure 3.5 Three design cases of the MH-PCM reactors proposed by Mellouli et al. [85]	25
Figure 3.6 Comparison of reacted hydrogen fraction (a) and melted PCM fraction (b) for three different design cases from Figure 3.5 studied by Mellouli et al. [85]	25
Figure 3.7 Schematic drawing of a base case: (a) cross-sectional and (b) 2D axisymmetric views	28
Figure 3.8 2D axisymmetric computational models showing 1 mm (a), 3 mm (b) and 5 mm (c) thicknesses of embedded copper fins between the MH and the PCM layers	28
Figure 3.9 2D axisymmetric computational models of 10 sandwich layers of the MH and PCM beds, Design #2, (a) and 10 sandwich layers of the MH-Fin-PCM, Design #3 (b)	30
Figure 3.10 Cross-sectional contours of average temperature (a) and reaction fraction (b) during the hydrogen absorption reaction for the base case at 100 s, 2000 s, 4000 s and 6000 s	36
Figure 3.11 Cross-sectional contours of average temperature (a) and reaction fraction (b) during the hydrogen desorption reaction for the base case at 100 s, 2000 s, 7000 s and 15000 s	38
Figure 3.12 Hydrogen mass fraction during hydrogen absorption (a) and desorption reactions (b) for each improved reactor designs	42
Figure 3.13 Liquid fraction during hydrogen absorption (a) and desorption (b) reactions for each improved reactor design.	42
Figure 3.14 Hourly average ambient temperature recorded in Randwick, Sydney, New South Wales, Australia, on 1/Oct/2023 [94]	45

Figure 3.15 Average MH & bed temperature (top) and PCM liquid fraction & hydrogen mass fraction (bottom) during total five continuous absorption and desorption periods for design #3. Shaded and unshaded areas indicate hydrogen absorption and desorption reactions, respectively.	47
Figure 3.16 Ambient temperature and average MH bed temperature during 68 cycles of absorption and desorption reactions for Design #3	49
Figure 3.17 Ambient temperature and average PCM bed temperature during 68 cycles of absorption and desorption reactions for Design #3	49
Figure 3.18 Average temperature of MH and PCM beds of Design #3 at the end of each absorption and desorption reaction along with ambient temperature during 68 cycles	50
Figure 3.19 Hydrogen mass fraction along with ambient temperature during 68 cycles for Design #3	51
Figure 3.20 PCM liquid fraction along with ambient temperature during 68 cycles for Design #3	52
Figure 3.21 Maximum and minimum hydrogen fraction and PCM liquid fraction during each absorption and desorption cycle along with ambient temperature during 68 cycles for Design #3	52
Figure 3.22 Operational time during each absorption and desorption cycle along with ambient temperature	53
Figure 4.1 Overall methodology of the current chapter	59
Figure 4.2 A helical coil with parameter names	60
Figure 4.3 3D models of MH hydrogen storage reactors with different internal helical coil dimensions: 1 coil turn, 60 mm axial pitch, 12 mm coil radius and 4 mm coil pipe radius (a), 6 coil turns, 30 mm axial pitch, 10 mm coil radius and 6 mm coil pipe radius (b), 9 coil turns, 30 mm axial pitch, 15 mm coil radius and 2 mm coil pipe radius (c)	61

Figure 4.4 Relationship between the hydrogen absorption time and coil design parameters – axial pitch (a), pipe radius (b), number of coil turn (c), velocity of water (d) and coil radius (e), and a correlation heatmap between variables (f)	67
Figure 4.5 Cross-sectional contours of temperature and hydrogen mass fraction at 100 s, 250 s, and 380 s for four sampled cases with different parameters	69
Figure 4.6 R^2 for different regression models to predict hydrogen absorption time	72
Figure 4.7 MAE for different regression models to predict hydrogen absorption time	72
Figure 4.8 MAPE for different regression models to predict hydrogen absorption time	73

List of Table

Table 3.1 Properties of four different PCMs [70]	21
Table 3.2 Thermochemical properties of MH and PCM	27
Table 3.3 Geometrical properties of the base case	27
Table 3.4 Hydrogen reaction time during absorption and desorption reactions for all the design cases, and improvement rates in the reaction time compared to that of the base case	43
Table 3.5 Final liquid fraction for all the design cases	43
Table 4.1 Design parameters range for the MH hydrogen storage reactor with the internal helical coil for machine learning analysis	61
Table 4.2 A sample dataset for machine learning analysis	62

List of Nomenclature

C_a	Absorption rate (s^{-1})
C_d	Desorption rate (s^{-1})
C_p	Specific heat capacity (J/kg K)
E	Activation energy (J mol^{-1})
H	Enthalpy (J/kg)
$\frac{H}{M}$	Hydrogen to metal atomic ratio
ΔH	Reaction heat of formation (J kg^{-1})
K	Permeability (m^2)
k	Thermal conductivity ($\text{W m}^{-1} \text{K}^{-1}$)
L	Latent heat (J/kg)
M	Metal
p	Pressure (bar)
R	Universal gas constant ($\text{J/mol}_{\text{H}_2}\text{K}$)
T	Temperature (K)
t	Time (s)

Greek symbols:

ε	Porosity
ρ	Density (kg/m^3)
\vec{u}	Velocity factor (m/s)
μ	Dynamic viscosity (kg/m K)

Subscripts:

0	Initial
a	Absorption
d	Desorption
eff	Effective
emp	Empty
	XIII

<i>eq</i>	Equilibrium
<i>in</i>	Inlet
<i>out</i>	Outlet
<i>m</i>	Metal
<i>sat</i>	Effective
<i>ref</i>	Reference

Superscripts:

<i>g</i>	Gaseous phase
<i>l</i>	Liquid phase
<i>mel</i>	Melting point
<i>p</i>	Phase-Change-Material
<i>s</i>	Solid phase

Chapter 1 Introduction

1.1. Background

Net-zero emissions are already a global trend to minimise carbon emissions as much as possible to prevent global warming and climate risks. Hydrogen, on the other hand, is considered a fuel of the future due to its abundance, sustainability, and environmental friendliness. [1, 2] Along with hydrogen production, much research is ongoing on storage in metal hydrides (MH), metal-organic frameworks, and a liquid state. Compared to other hydrogen storage methods, MHHSS operates at moderate temperatures and pressures and has higher storage density, which makes it promising. [3, 4] Typical MHHSS involves reactions between hydrogen and porous MH beds. For example, hydrogen molecules are attached to and detached from MH beds during absorption and desorption reactions, respectively. Lanthanum nickel (LaNi_5) is a widely chosen metal in MHHSS due to its better kinetics, moderate operating temperatures, and good reversibility. [4]

MHHSS still has critical drawbacks compared to other storage methods, such as low gravimetric capacity and slower kinetics. [5] However, these disadvantages can be optimised with efficient thermal management systems as thermophysical properties are key driving factors for MHHSS. For example, the difference between system and equilibrium pressure drives hydrogen absorption and desorption reactions. Equilibrium pressure itself is then dependent on operating temperature and pressure.

In addition, hydrogen absorption and desorption reactions are exothermic and endothermic, respectively. Therefore, keeping the temperature low and high for absorption and desorption reactions, respectively, is necessary with effective thermal management systems.

Optimising MHHSS through conventional experiments takes significant time, expenditure, and resources. However, due to its cost-effectiveness and instant nature, CFD is an efficient tool for optimising MHHSS designs and analysing thermophysical phenomena. As shown in Figure 1.1, a typical CFD process involves modelling of geometry, followed by meshing of the geometry. Then, numerical conditions, such as initial and boundary conditions, are applied to the model. CFD solves these numerical conditions by solving mass, momentum, and energy conservation equations through iterative processes until convergence. Once equations are solved, results are analysed by post-processing.

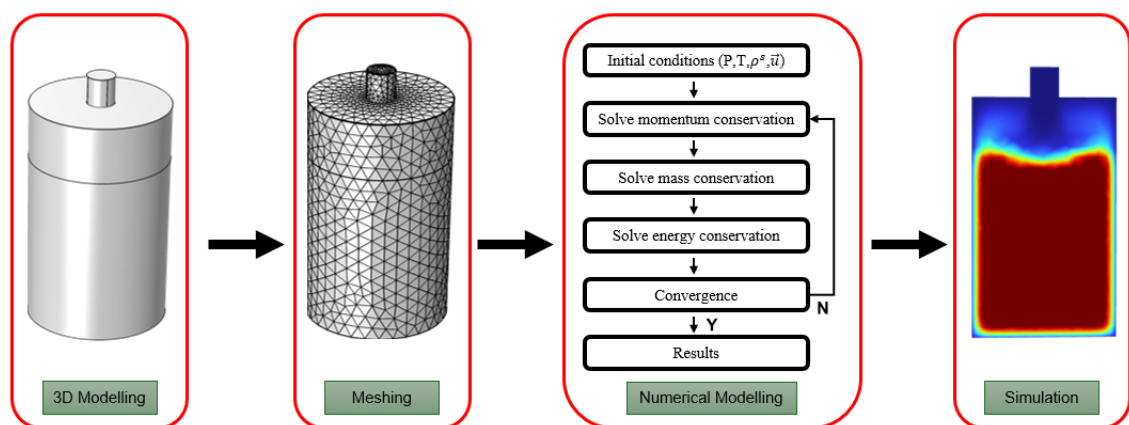


Figure 1.1 Visualisation of a typical CFD process

1.2. Objective

This thesis mainly focuses on the design optimisation of MHHSS to overcome its disadvantages, such as low gravimetric storage density and slower kinetics. To enable cost-effective and efficient approaches, design optimisation is proceeded by CFD. In the first numerical simulation, MHHSS is optimised with sandwich-layered PCM-Fin-MH configuration to enhance reaction rates and reversibility. The PCM-Fin-MH system is then tested as an independent system that does not require conventional HTFs, which can be extended to industrial applications. The following chapter involves the ML approach to predict the hydrogen absorption time given different coil design parameters. This aims to prove that ML-integrated CFD analysis in MHHSS is robust and can be extended to industrial applications.

1.3. Thesis Organisation

As per the aims discussed in the section 1.2, this thesis is organised as shown in Figure 1.2. **Chapter 2** discusses in-depth background information on MHHSS that is foundational to the overall studies of this thesis, such as reaction mechanisms, experimental optimisation and numerical optimisation. **Chapter 3** evaluates an optimised MHHSS with PCM and copper fins and discusses its effectiveness in hydrogen absorption and desorption reactions. It also analyses the reversibility of MH-Fin-PCM configuration and potential application as an independent system without conventional HTFs.

In **Chapter 4**, ML is integrated into CFD analysis to predict hydrogen absorption time given different coil design parameters. The aim is to prove the potential applications of ML to CFD in MHHSS fields while maximising the benefits of both ML and CFD. **Chapter 5** summarises key results and findings throughout this thesis and discusses potential future applications of MHHSS.

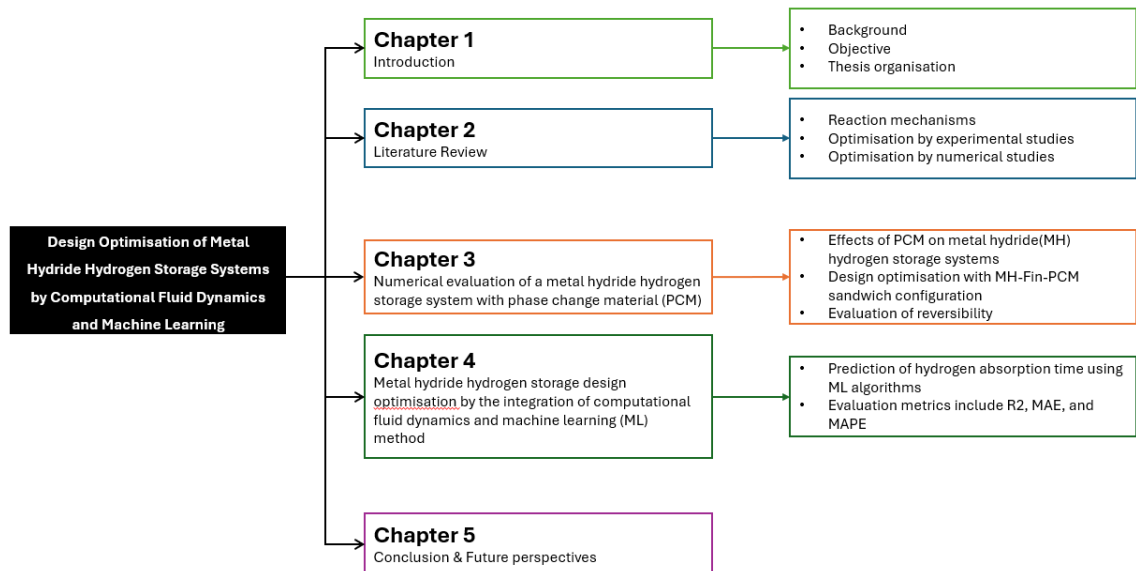


Figure 1.2 Overall thesis organisation

Chapter 2 Literature Review

This chapter addresses essential background information for MHHSS that is foundational throughout this thesis. Firstly, reaction mechanisms for hydrogen absorption and desorption reactions are discussed in Reaction Mechanisms. It addresses mathematical formulae of mass and heat transfer phenomena during these reactions. Then, design optimisations of MHHSS through experiments are addressed in Experimental Optimisation. Lastly, the effectiveness of CFD for design optimisations of MHHSS is highlighted in Numerical Optimisation.

2.1. Reaction Mechanisms

A reversible reaction of hydrogen and a metal alloy forms MH, expressed as follows, where M is a metal alloy and ΔH is the heat of reaction. [6]



Overall reactions between hydrogen and a metal alloy within MHHSS can be expressed in mass, momentum, and energy conservation equations. For example, the mass conservation equation describes the distribution of the hydrogen concentration as time evolves. The mass balance equations for hydrogen and a metal alloy are expressed in Eq. 2 and Eq.3, respectively.

$$\frac{\partial \epsilon \rho^g}{\partial t} = \nabla \cdot (\rho^g \vec{u}) = -S_m \quad (2)$$

$$(1 - \epsilon) \frac{\partial \rho^s}{\partial t} = S_m \quad (3)$$

In Eq. 2 and Eq.3, ε refers to the porosity of MH and S_m refers to the mass source term indicating the rate of absorbed or desorbed hydrogen mass per unit volume.

In 1980, Suda and Kobayashi [7] defined the mass source term as functions by testing various metal alloys, including LaNi_5 . As shown in Eq. 4 and Eq. 5, these functions have been elaborated and used by other studies. [8–11]

$$S_{m,a} = C_a \exp\left(-\frac{E_a}{R^g T}\right) \ln\left(\frac{P^g}{P_{eq,a}}\right) (\rho_{sat}^s - \rho^s) \quad (4)$$

$$S_{m,d} = C_d \exp\left(-\frac{E_d}{R^g T}\right) \left(\frac{P^g - P_{eq,d}}{P_{eq,d}}\right) (\rho^s - \rho_{emp}^s) \quad (5)$$

In Eq. 4 and Eq. 5, ρ_{sat}^s refers to the density of the MH bed saturated with hydrogen and ρ_{emp}^s refers to the hydrogen-free density of the MH bed. C_a and C_d refer to reaction rate constants for absorption and desorption reactions, respectively. E_a and E_d refer to activation energy for absorption and desorption reactions, respectively. Jemni and Ben Nasrallah [11, 12] proposed C_a and C_d for LaNi_5 to be 59.187 s^{-1} and 9.57^{-1} , respectively, and E_a and E_d to be 21179.6 J/mol and 16473 J/mol , respectively.

Equilibrium pressure, P_{eq} , is a key driving factor for hydrogen absorption and desorption reactions, as shown in Eq. 4 and Eq. 5. It is described by Pressure-Composition-Temperature (PCT) curve, Figure 2.1, showing its relationship to concentration of hydrogen in the MH bed and temperature. The hydrogen absorption reaction starts with the α stage with a low concentration of hydrogen. It begins to dissolve into the metal, gradually increasing equilibrium pressure. Once it reaches the limiting solubility, it reaches the β stage, where equilibrium pressure remains constant due to a phase change, and massive hydrogen is absorbed.

The length of the constant equilibrium pressure line, or plateau line, determines the performance of a metal alloy. Since the hydrogen absorption reaction is exothermic, and the length of the plateau line decreases as temperature increases, keeping the MHHSS temperature low drives the reaction faster. Similarly, as the hydrogen desorption reaction is endothermic, keeping the MHHSS temperature high drives the reaction faster.

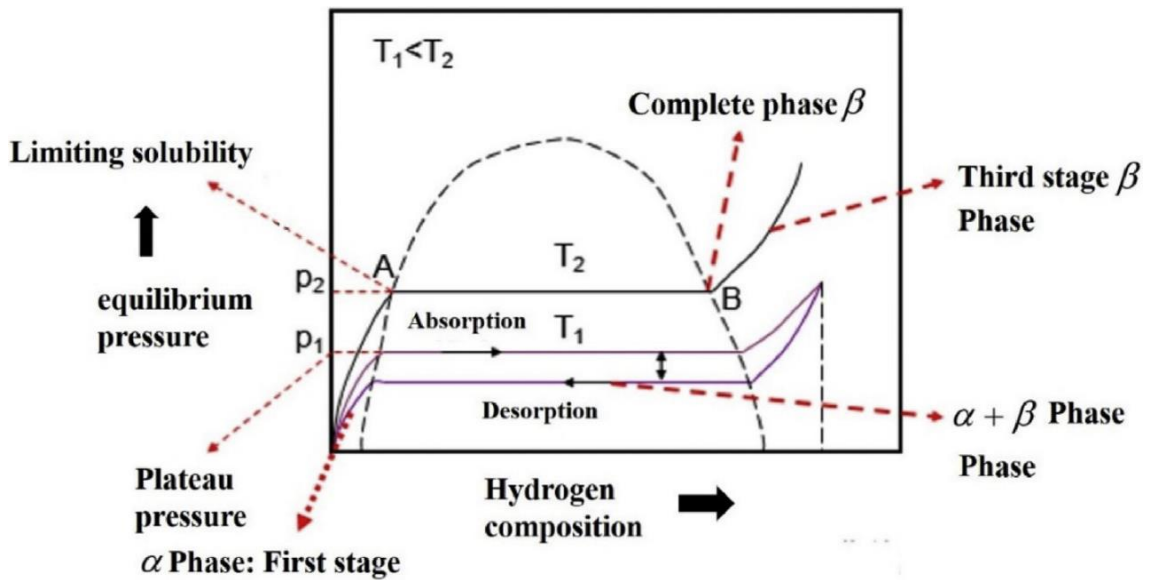


Figure 2.1 PCT curve of a typical MH

Jemni et al. [10, 11] proposed the equilibrium pressure as a function of 5th, 7th, and 9th order polynomials based on the van't Hoff equation, as shown below. $\frac{H}{M}$ refers to the hydrogen to metal atomic ratio. Different values of the coefficient, a_n , have been proposed. Jemni et al. [11–13] and Dhaou et al. [14] suggested these coefficients for the hydrogen absorption and desorption reactions, respectively, from experiments.

$$P_{eq} = \left(\sum_{n=0}^{\infty} a_n \left(\frac{H}{M} \right)^n \right) \exp \left[\frac{\Delta H}{R_g} \left(\frac{1}{T} - \frac{1}{T_{ref}} \right) \right] \quad (6)$$

The motion of hydrogen is expressed in the Navier-Stokes equations, as shown in Eq. 7.

It is also referred to as the momentum conservation equation and has been applied to various studies. [15–17]

$$\frac{1}{\varepsilon} \left[\frac{\partial \rho^g \vec{u}}{\partial t} + \frac{1}{\varepsilon} \rho^g (\vec{u} \cdot \nabla) \vec{u} \right] = \nabla \cdot (-p + \tau) + S_u \quad (7)$$

$$\tau = \vec{u} \frac{1}{\varepsilon} (\nabla \vec{u} + (\nabla \vec{u})^T) - \frac{2}{3} \vec{u} \frac{1}{\varepsilon} (\nabla \cdot \vec{u}) \quad (8)$$

In Eq. 7, S_u refers to the volumetric momentum source based on Darcy's law in terms of permeability (K) and the dynamic viscosity (μ).

$$S_u = -\frac{\mu}{k} \vec{u} \quad (9)$$

The energy conservation equation can express energy flow and heat transfer, assuming local thermal equilibrium between hydrogen and the MH bed. Jemni and Ben Nasrallah [11, 12] derived a single equation, Eq.10, to avoid negligible terms.

$$\frac{\partial \overline{\rho C_p T}}{\partial t} + \nabla \cdot (\rho^g C_p^g \vec{u} T) = \nabla \cdot (k^{eff} \nabla T) + S_T \quad (10)$$

$$\overline{\rho C_p} = (1 - \varepsilon) \rho^s C_p^s + \varepsilon \rho^g C_p^g \quad (11)$$

$$k^{eff} = (1 - \varepsilon) k^s + \varepsilon k^g \quad (12)$$

In Eq.10, S_T refers to the volumetric energy source term, expressed in Eq. 13.

$$S_T = S_m[\Delta H - T(C_p^g - C_p^s)] \quad (13)$$

These mathematical formulae suggest that the reaction mechanisms of hydrogen absorption and desorption reactions are highly related to pressure and temperature. Therefore, efficient design optimisations of MHHSS are critical to enhance its performance. Researchers have studied various methods to optimise MHHSS both experimentally and numerically, which are discussed in the Experimental Optimisation and Numerical Optimisation, respectively.

2.2. Experimental Optimisation

Early designs of MHHSS included cylindrical reactors with surrounding jackets where HTF flows, as shown in Figure 2.2. [13, 18–20] Jemni et al. [13] experimentally studied the LaNi₅-H₂ system to derive its equilibrium pressure, reaction rate, and effective thermal conductivity. Muthukumar et al. [20] also studied the cylindrical reactor with the jacket and observed that lower HTF temperatures result in faster hydrogen absorption reactions. However, such designs have poor heat transfer surface area, especially around the inner core region. For example, Jemni et al. [13] studied the similar design of MHHSS, Figure 2.3(a), and measured temperatures at three different locations. It was observed that once the MH bed reaches the maximum temperature, location C recorded the fastest drop in temperature due to surrounding cooling water, followed by locations B and C. Compared to location C, location A has poor heat transfer with the surrounding HTF, resulting in relatively higher bed temperatures and slower reaction rates.

2.2 EXPERIMENTAL OPTIMISATION

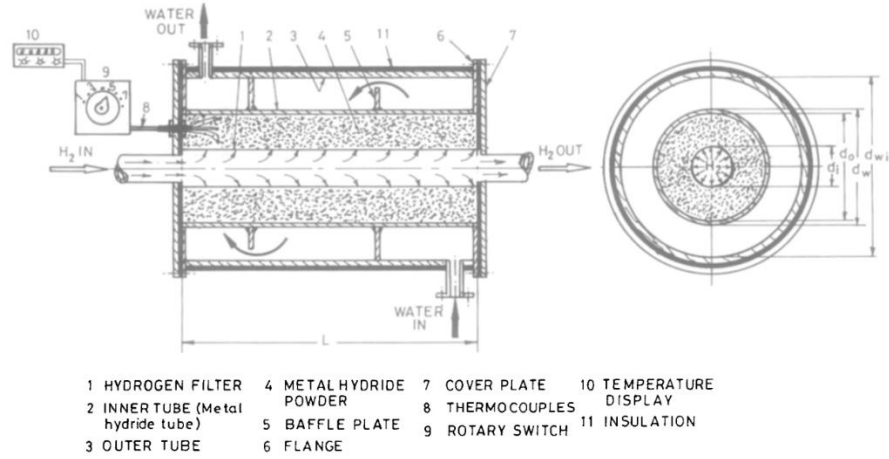


Figure 2.2 An early design of MHHSS including cylindrical reactors and surrounding jackets studied by Ram Gopal and Srinivasa Murthy [18]

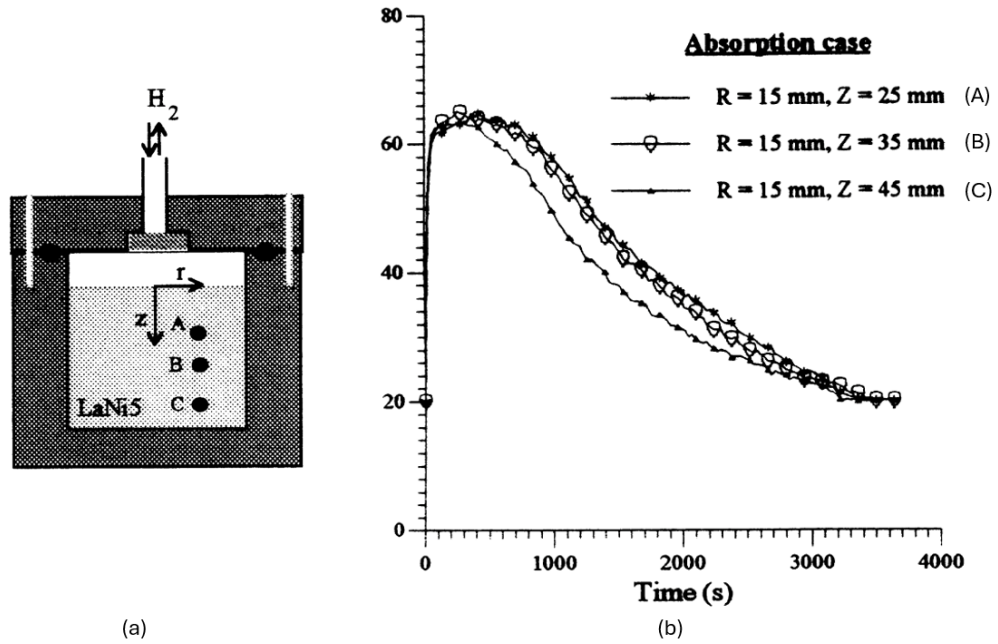


Figure 2.3 Experimental measurements of temperature at three different locations by Jemni et al. [13]

Several other studies have involved MHHSS with internal heat transfer pipes to enhance heat transfer across the entire MH bed. [21–24] Anbarasu et al. [24] compared MHHSS with 36 and 60 internal heat transfer pipes, observing the higher number of internal heat transfer pipes enhances the hydrogen absorption time due to better heat transfer surface area.

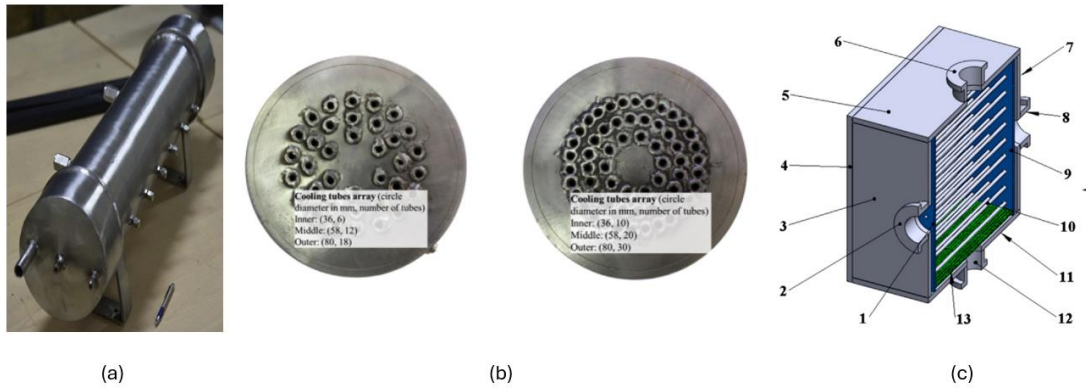


Figure 2.4 MHHSS with internal heat pipes studied by Kumar et al. [21] (a), Anbarasu et al. [24] (b), and Meng et al. [23] (c)

2.3. Numerical Optimisation

Conventional experiments have critical disadvantages regarding design optimisations as they require extensive resources, time, and scale limitations. However, numerical modelling can handle them due to their cost-effectiveness and rapid nature, and it is highly effective in analysing internal heat and mass transfer within MHHSS.

MHHSS with internal straight heat transfer pipes were also studied numerically. [25–30] Muthukumar et al. [25] compared numerical modellings of MHHSS with 12, 14, 16, 18 and 20 internal straight heat transfer pipes and observed internal heat distribution phenomena, concluding the reactor with 20 internal straight heat transfer pipes performs the most superior. As shown in Figure 2.5, Krokos et al. [30] studied effects of different distribution configurations of 9 internal straight heat transfer pipes and observed that even distribution, Figure 2.5(e), results in the most efficient heat transfer and the fastest reaction. Bhouri et al. [27] further optimised the MHHSS by including honeycomb-like, or hexagonal, heat transfer pipes instead of the conventional cylindrical shape.

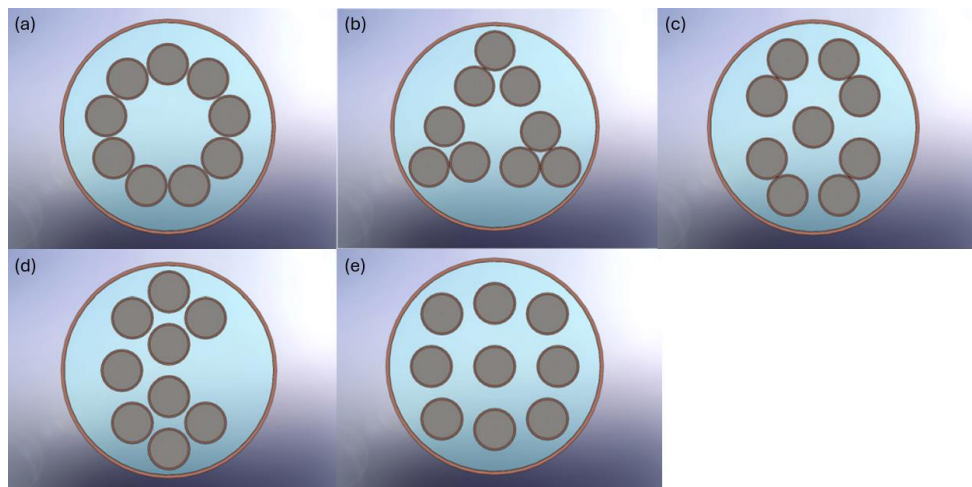


Figure 2.5 MHHSS with 9 internal straight heat transfer pipes with different distribution configurations studied by Krokos et al. [30]

Numerical studies have allowed further optimisations of internal heat transfer pipes. For example, several studies involved U-shaped heat transfer tubes instead of straight pipes. [31–34] Additionally, internal helical coils have significantly enhanced the MHHSS performance due to the increased effective heat transfer surface area. [35–46]

Wu et al. [43] compared numerical MHHSS models with the internal straight pipe and the internal helical coil as shown in Figure 2.6(a) and Figure 2.6(b), and observed that the reactor with the helical coil performs faster hydrogen absorption reaction due to enhanced heat and mass transfer. Wang et al. [45], Figure 2.6(c), numerically studied effects of internal coil parameters on the MHHSS performance. This study highlighted that higher coil diameter, shorter coil pitch, and higher tube diameter lead to faster hydrogen reaction due to increased heat transfer surface area. Wang et al. [46], Figure 2.6(d), studied with improved and more complex designs of straight pipes and coils. They concluded that the radiation tube improved reaction time by 77%, 52%, and 37% compared to no internal heat pipe, straight tube, and spiral tube, respectively.

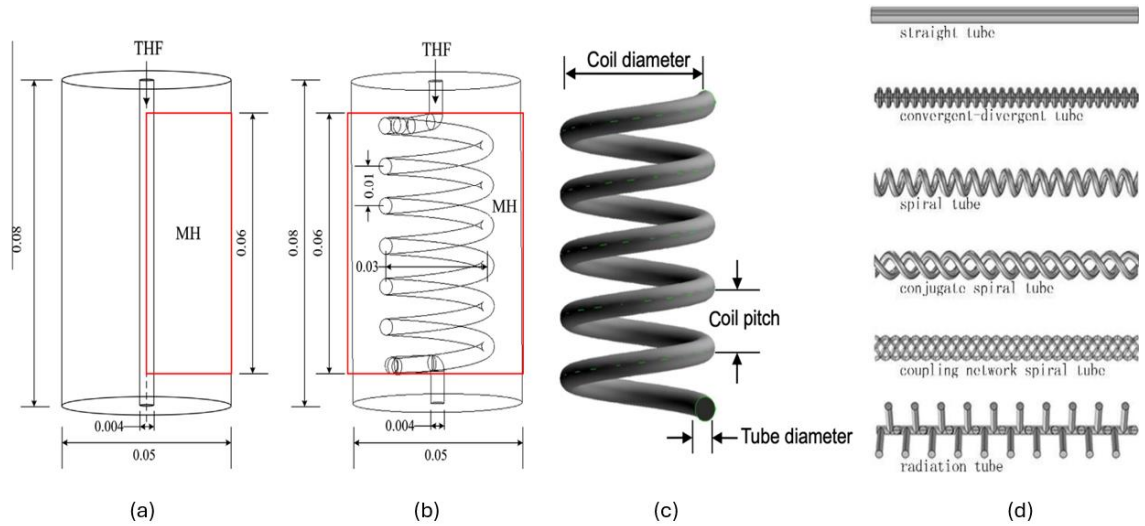


Figure 2.6 MHHSS with the internal straight pipe (a) and the helical coil (b) studied by Wu et al. [43] Different coil parameters studied by Wang et al. [45] (c) Various complex designs of internal heat pipes studied by Wang et al. [46] (d)

Several other studies optimised MHHSS by improving thermal conductivity between HTF and the MH bed. For example, some designs included embedded fins made of a high thermal conductivity material, such as copper. [31, 38, 39, 41, 47–59] Kaplan [54] compared a MHHSS without any design improvement and with external circular fins embedded to the reactor wall, as shown in Figure 2.7(a) and Figure 2.7(b), respectively, and observed that the reactor with embedded circular fins performed more efficient heat removal and the faster absorption reaction. In addition to similar reactors shown in Figure 2.7(a) and Figure 2.7(b), Askri et al. [47] additionally compared MHHSS with the internal heat transfer pipe and with internal fins embedded to the internal heat transfer pipe, as shown in Figure 2.7(c) and Figure 2.7(d), respectively. They concluded that compared to MHHSS without any design improvement, reactors shown in Figure 2.7(b), Figure 2.7(c), and Figure 2.7(d) improved the hydrogen absorption time by 10%, 56%, and 80%, respectively.

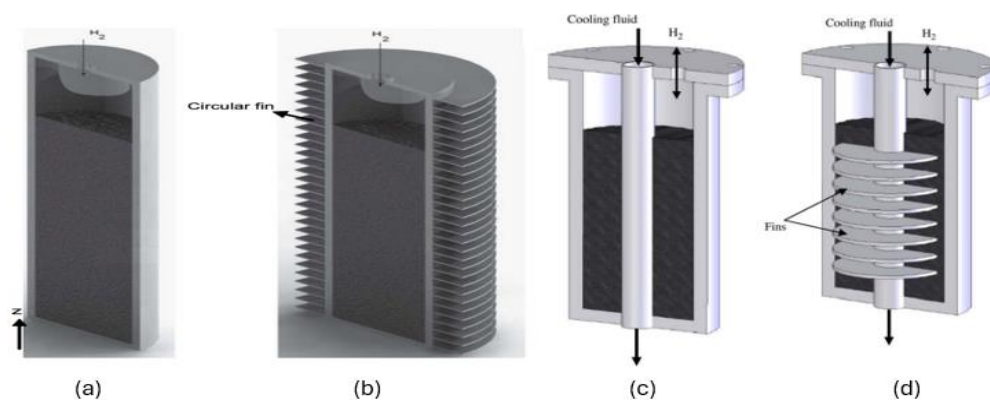


Figure 2.7 MHHSS without any design improvement (a), with external circular fins (b), with an internal heat transfer pipe (c), and with an internal heat transfer pipe and internal embedded fins [47, 54]

Several researchers studied the reactors fins embedded to helical coils to further enhance the heat transfer between the MH bed and HTF within the helical coils. [38, 39, 41] Shouahlia et al. [41] compared two MHHSS, one with fins embedded to a single internal straight heat transfer pipe and the other with fins embedded to an internal spiral coil. They observed a significant improvement in the hydrogen absorption time and the heat recovery rate for the MHHSS with fins embedded to an internal spiral coil. Mellouli et al. [39] compared four different designs of internal heat exchange systems of MHHSS – Figure 2.8(a): a single internal helical coil, Figure 2.8(b): circular fins embedded to a single internal helical coil, Figure 2.8(c): double internal helical coils, and Figure 2.8(d): concentric fins embedded to double internal helical coils. They observed that the fins enhanced the heat transfer between the MH bed and the heat transfer pipes as the temperature gradient between the HTF and fins in Figure 2.8(b) were higher than that between the HTF and the MH bed in Figure 2.8(a). Additionally, they concluded that MHHSS designs of Figure 2.8(b), Figure 2.8(c), and Figure 2.8(d) improved 16%, 65%, and 70%, respectively, in the hydrogen absorption time compared to the base design, Figure 2.8(a).

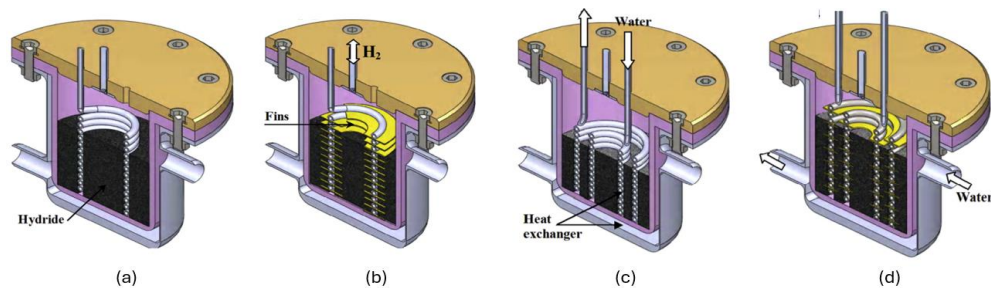


Figure 2.8 Four different designs of internal heat transfer systems of MHHSS studied by Mellouli et al. [39]

Optimised designs of fins have further improved the MHHSS performance. [28, 50, 52, 53, 58, 59] Garrison et al. [48] compared two different fin configurations, transverse and longitudinal, and concluded that longitudinal fins resulted in slightly more efficient heat transfer and the overall hydrogen absorption reaction rate. Bhourri et al. [28] examined the effects of fin thickness and the number of fins embedded to a single internal heat transfer pipe. They concluded that higher fin thickness and higher number of fins resulted in a faster reaction time. Bai et al. [50] compared effects of radial fins, unoptimized tree-shaped fins, and optimised tree-shaped fins as shown in Figure 2.9. They observed an improvement of 7% and 20.7% in the hydrogen charging time for the unoptimized tree-shaped fins and the optimised tree-shaped fins, respectively, compared to radial fins.

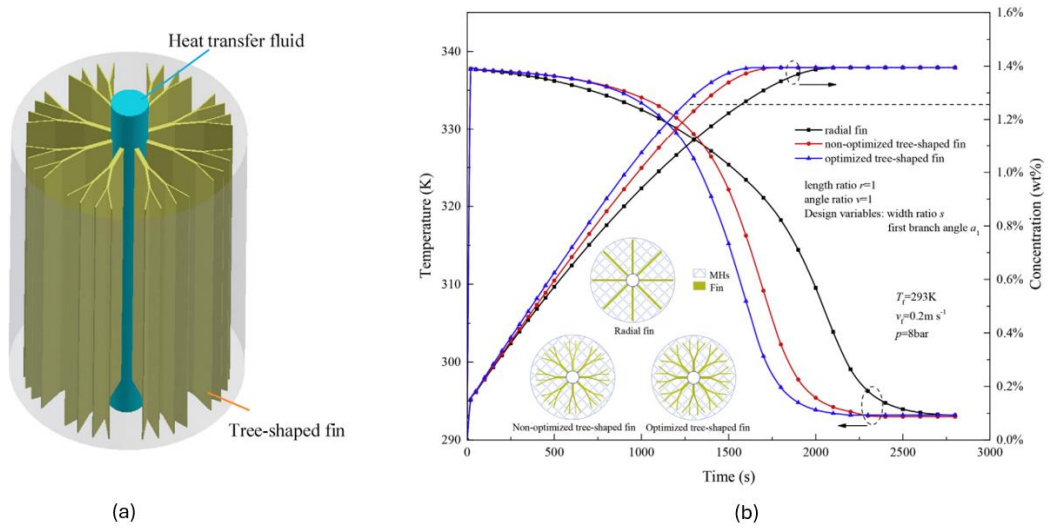


Figure 2.9 Three different designs of fins (a) and their effects on the hydrogen absorption time (b) studied by Bai et al. [50]

Additionally, several complex geometries of fins have been proposed. [53, 58–61] Raju et al. [58], Visaria et al. [53], and Keshari et al. [59] studied effects of operating conditions on the MHHSS performances using complex geometries of internal straight heat transfer pipes and fins, as shown in Figure 2.10(a), Figure 2.10(b), and Figure 2.10(c), respectively. George et al. [60] and Afzal et al. [61] proposed honeycomb-shaped configurations, as shown in Figure 2.10(d) and Figure 2.10(e), respectively, to further optimise the arrangements of fins and heat transfer pipes and observed improvements in the hydrogen reaction rates.

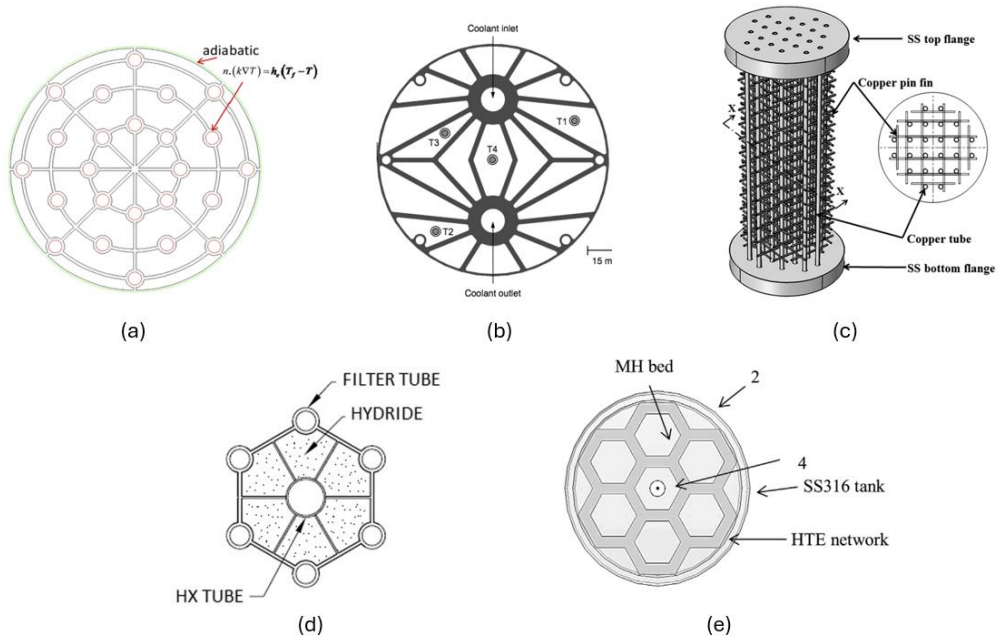


Figure 2.10 Complex geometries of fins [53, 58–61]

In addition to fins, several studies included metal foams, such as aluminium, copper, and zinc, to the MHHSS to further enhance the thermal conductivity. [17, 62–67] Laurencelle and Goyette [63] studied the effects of 91% porosity of aluminium foam and observed an increase of thermal conductivity from $0.15 \text{ W/m}\cdot\text{K}$ to $10 \text{ W/m}\cdot\text{K}$ by including aluminium copper foams, which enhanced the hydrogen sorption rate by 7.5 times compared to the MHHSS without aluminium foams. Wang et al. [66] also compared a MHHSS without any foams, with 5% and 10% aluminium foams, and observed 28.2% and 38.4% improvements in the hydrogen sorption rates by adding 5% and 10% aluminium foams, respectively, compared to the MHHSS without any foams. Zhuo et al. [17] studied the MHHSS with aluminium foams encapsulating copper fins embedded to internal straight cooling tubes and observed a 16.7% improvement in the hydrogen desorption time by adding aluminium foams.

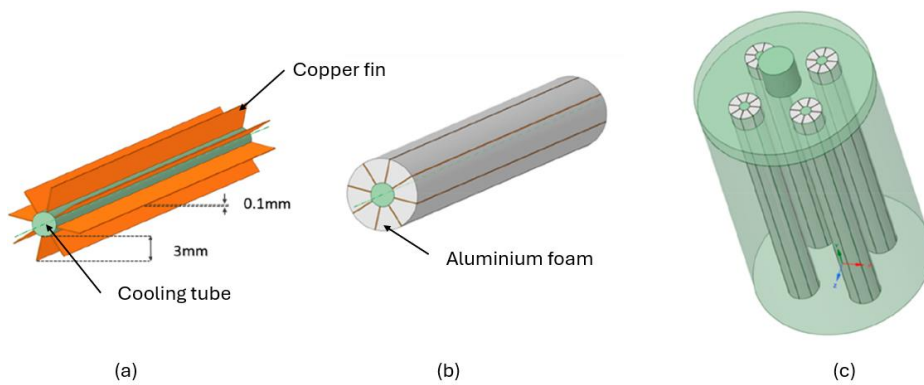


Figure 2.11 A study of the effect of aluminium foam on the hydrogen desorption rate conducted by Zhuo et al. [17]

2.4. Knowledge Gaps

As introduced throughout the **Chapter 2**, the MHHSS requires an efficient heat transfer management with the aid of HTFs. Therefore, constant supply of HTFs is compulsory, which additionally requires relevant resources. In addition, a requirement of constant supply of HTFs limits the MHHSS to be mostly stationary in the industry-scale facilities, which makes the MHHSS inefficient in the applications to moving vehicles or narrow spaces. Another limitation includes that the heat transfer between the MH bed and HTFs result in the potential waste of heat. For example, the endothermic hydrogen desorption reaction requires heat from HTFs, whereas the exothermic hydrogen absorption reaction requires to transfer heat to HTFs. These limitations can be moderated by integrating PCM to the MHHSS, which stores latent heat during the hydrogen absorption reaction and then can supply the stored heat to the MH bed during the hydrogen desorption reaction. The design optimisation of MHHSS with PCM is discussed in the **Chapter 3**.

Although CFD is effective in designing and predicting the performance of MHHSS relatively instantly and cost-effectively, it cannot predict unseen data. For example, when different design and operating parameters are required, another CFD case must be simulated. However, ML can predict CFD results with unseen data, which can be effective in choosing optimal operating and design parameters. Integration of ML and CFD can benefit from both advantages and will be highly effective in the industry applications. Therefore, in the **Chapter 4**, ML is integrated to predict the hydrogen absorption time given different design parameters of an internal helical coil within the MHHSS.

Chapter 3 Numerical evaluation of MHHSS with PCM

3.1. Introduction

Throughout the **Chapter 2**, the importance of efficient thermal management with HTFs as cooling and heating media is highlighted. However, this conventional heat transfer management with HTFs has a few drawbacks, including waste of heat and requirements of relevant resources to build and constantly supply HTFs to the MHHSS. However, PCM can handle such drawbacks as an effective thermal management system.

With the high thermal storage capacity, PCM has been widely used in various fields, such as solar energy, building and electronic devices. [68] In the MHHSS, PCM can store the generated heat during the exothermic hydrogen absorption reaction and can supply the stored thermal heat to the MH bed during the endothermic hydrogen desorption reaction. As illustrated in Figure 3.1, PCM changes its state from solid to liquid as it absorbs the latent heat from the MH bed during the hydrogen absorption reaction or supplies heat to the MH bed during the hydrogen desorption reaction.

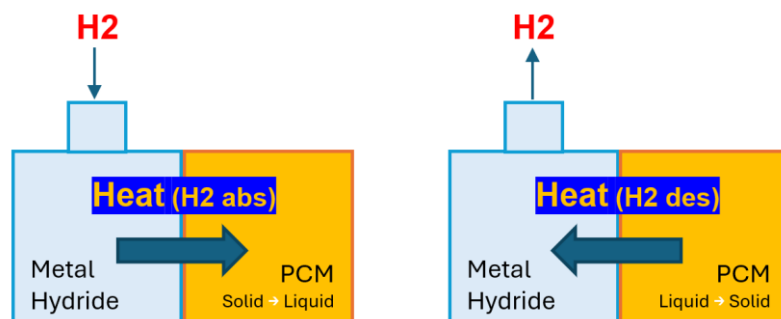


Figure 3.1 Illustration of heat transfer between MH and PCM beds during hydrogen sorption reactions

As PCM changes its states during the hydrogen sorption reactions, the choice of a PCM material in MHHSS highly depends on the melting temperature of PCM as it should lie between hydrogenation & dehydrogenation temperatures of the metal alloy. [69] The performance of the MHHSS with PCM also depends on its enthalpy of fusion as high enthalpy of fusion indicates PCM can absorb as much heat as possible with the minimum volume. [69] Such selection criteria for PCM are highlighted in the study by Mellouli et al. [70] They compared four different PCMs, NaOH, FeCl₃, NaNO₃ and KNO₃(10%)NaNO₃, to find a suitable PCM with Mg₂Ni as a metal alloy. As Mg₂Ni has the absorption and desorption temperatures at 617 K and 543 K, respectively, melting temperatures of these four PCMs also lie between this range, as shown in Table 3.1. As shown in Table 3.1 and Figure 3.2, higher enthalpy of fusion of a PCM, such as FeCl₃, allows its lower volume compared to the mass of Mg₂Ni. Mellouli et al. [70], however, selected NaNO₃ as a suitable PCM as FeCl₃ has a risk of corrosion and NaNO₃ still has a high enthalpy of fusion and occupies relatively low volume.

Table 3.1 Properties of four different PCMs [70]

Materials	Melting temperature (K)	Enthalpy of fusion (kJ/kg)	Density (kg/m ³)
NaOH	591	158	2100
FeCl ₃	582	267	2800
NaNO ₃	580	174	2260
KNO ₃ (10%)NaNO ₃	563	170	1700

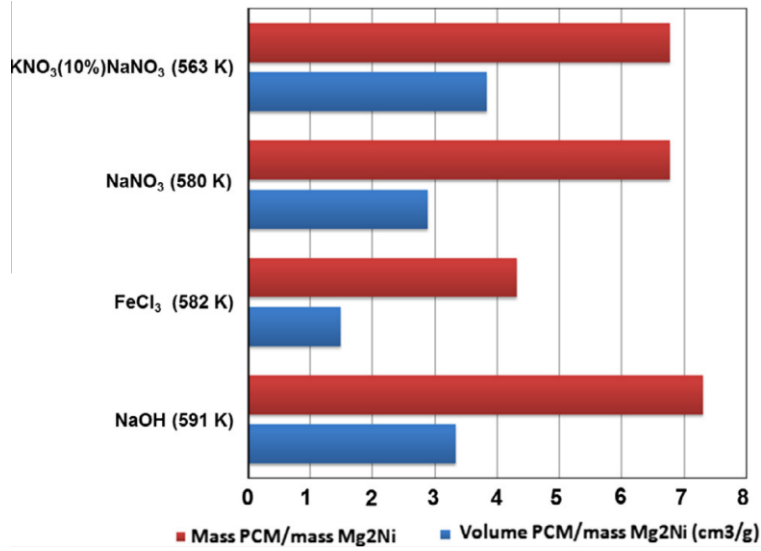


Figure 3.2 Mass and volume of PCMs and the MH bed studied by Mellouli et al. [70]

Integration of PCM to the MHHSS has also been widely studied and investigated often coupled with CFD. Several numerical studies analysed the MHHSS with a PCM bed and cooling jackets where the PCM bed simply surrounds the MH bed. [71–77] El Mghari et al. [73] numerically studied this simple MHHSS design with LaNi₅ as the metal and LiNO₃·3H₂O as a PCM. They observed that higher thermal conductivity and higher latent heat of the PCM resulted in the hydrogen sorption kinetics, but the latent heat of the PCM has more significant impact than the thermal conductivity. Several studies [71, 74] compared cylindrical and spherical configurations of the MH bed and the PCM bed and concluded that a spherical reactor design resulted in a better hydrogen sorption. Some studies [78–80] focused on the effects of embedded fins to enhance the heat transfer between the MH bed and the PCM beds and observed faster hydrogen reaction kinetics, as shown in Figure 3.3.

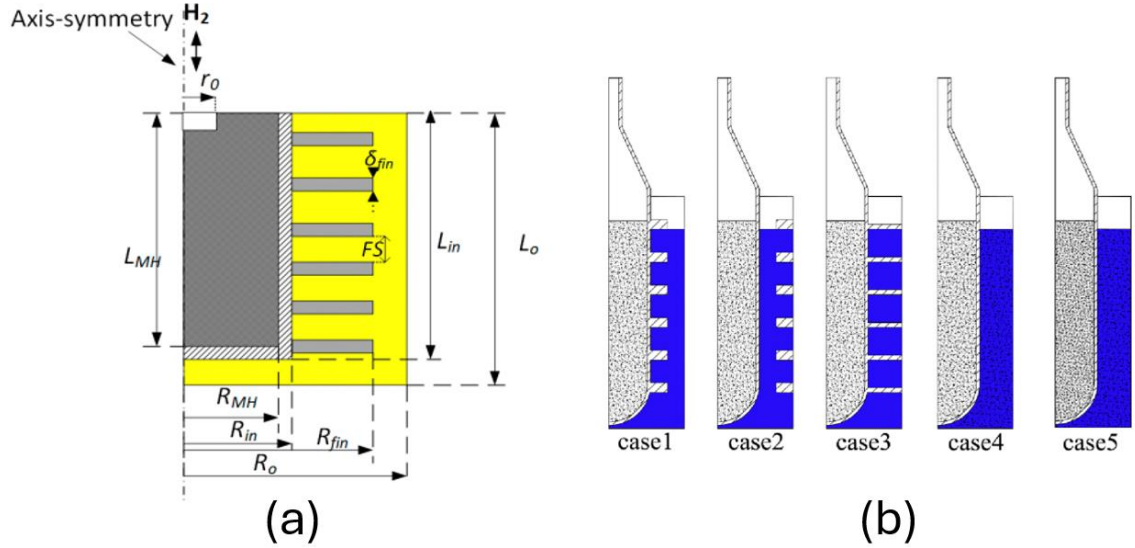


Figure 3.3 MHHSS with PCMs and embedded fins studied by Nyamsi et al. (a) and Yao et al. (b) [78, 80]

Several MHHSS designs with PCM highlighted the enhanced heat transfer surface area to improve the hydrogen sorption reactions. [70, 81–84] Alqahtani et al. [82] proposed MH-PCM sandwich bed where the MH bed is filled between the inner PCM and the outer PCM beds as shown in Figure 3.4(a). This configuration improved the hydrogen absorption and desorption time by 81.5% and 73%, respectively, compared to the conventional MH reactor with only one PCM bed. Hassan et al. [84] even increased the number of the MH-PCM layers, shown in Figure 3.4(b), and compared its performance with the one-layered MH-PCM reactor. They observed that the four-layered reactor had better capacity rate than the single-layered reactor and the hydrogen absorption time decreases as the thermal conductivity of PCM increases.

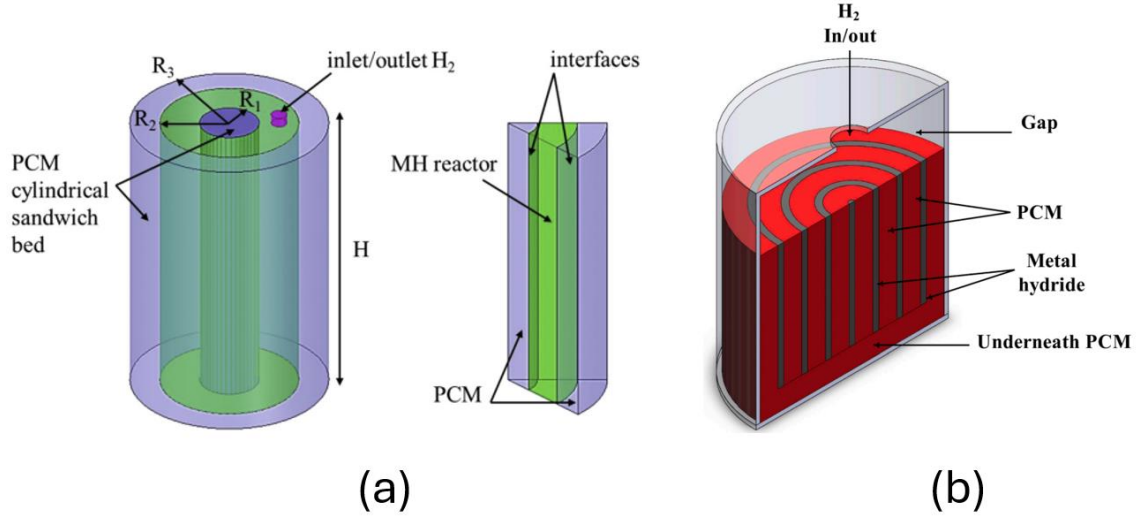


Figure 3.4 Sandwich configuration of MH and PCM beds studied by Alqahtani et al. (a) and Hassan et al. (b) [82, 84]

While the MHHSS in the abovementioned studies did not include conventional heat transfer pipes, several other studies included both internal heat transfer pipes and PCM layers. [85–87] Mellouli et al. [85] proposed three different designs of the MH-PCM reactors – a conventional reactor with the MH bed encapsulated by the PCM layer (case 1), additional twelve straight heat transfer pipes placed radially across the MH bed (case 2), and similar to the case 2, but equipped with U-shaped heat transfer pipes circulating across the MH and PCM beds (case3), as shown in Figure 3.5(a), Figure 3.5(b) and Figure 3.5(c), respectively. They observed that case 2 and case 3 improved the hydrogen filling time by 94% and 72%, respectively, compared to case 1, as shown in Figure 3.6(a). However, most of the heat generated by the MH bed in case 2 transferred to the heat transfer pipes and was wasted, which caused its PCM bed to barely react, as shown in Figure 3.6(b). This study suggested that, depending on the priorities, the usage of the heat transfer pipes and the PCM should be balanced for the MH-PCM reactor.

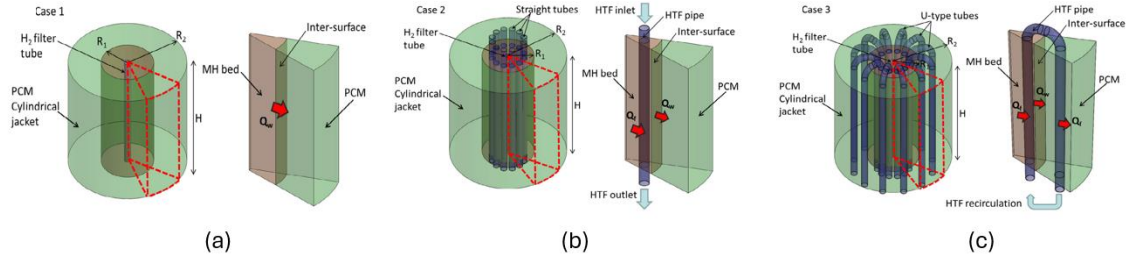


Figure 3.5 Three design cases of the MH-PCM reactors proposed by Mellouli et al. [85]

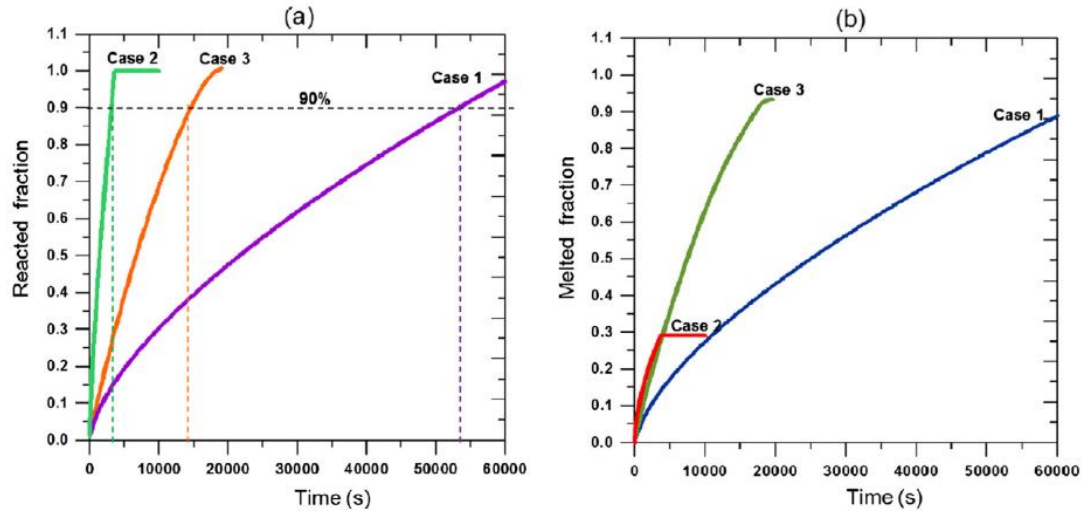


Figure 3.6 Comparison of reacted hydrogen fraction (a) and melted PCM fraction (b) for three different design cases from Figure 3.5 studied by Mellouli et al. [85]

From various studies discussed so far, using PCMs can replace the conventional heat transfer pipes and HTFs, although the reaction rate for a MH-PCM reactor could be slower than a MH reactor with heat transfer pipes and HTFs. However, as stated, the usage of PCMs instead of HTFs can be economical and allows the MH-PCM reactor to be used in confined spaces or moving vehicles. This chapter discusses the optimised design of the MH-PCM reactor by sandwich layers of MH-Fin-PCM, and the reversibility of this proposed design under the actual recorded ambient temperature.

3.2. Model Description

In this study, four different models of a MH-PCM reactor were numerically evaluated. These models are transient and 2D axisymmetric, considering that the symmetric geometry allows faster computational time with less computational costs. For the MH bed and the PCM bed, lanthanum nickel (LaNi_5) and lithium nitrate trihydrate ($\text{LiNO}_3 \cdot 3\text{H}_2\text{O}$), respectively, were selected. As mentioned earlier, the melting temperature of a PCM must be lie between the absorption and desorption temperatures of a metal alloy. LaNi_5 operates between 293 K and 353 K, whereas the melting temperature of $\text{LiNO}_3 \cdot 3\text{H}_2\text{O}$ is at 303 K, which satisfy the operating conditions of a MH-PCM reactor. [88, 89] Thermochemical properties of MH and PCM are listed in the Table 3.2.

3.2.1. Base case

The base case is an unoptimized MH-PCM reactor where the inner cylinder is filled with the MH bed and the outer cylinder is filled with the PCM bed, as shown in Figure 3.7. This model was developed for the model validation against studies by Ben Mâad et al. [90] and El Mghari et al. [73] for the absorption and desorption reaction, respectively. The base case was also used to evaluate the internal heat and mass transfer across the reactor. In addition, this model was compared by three other optimised MH-PCM designs, introduced in the sections 3.2.2 and 3.2.3, to evaluate improvements in the optimised designs. Geometrical properties of the base case are listed in the Table 3.3.

Table 3.2 Thermochemical properties of MH and PCM

Description	Value	Ref.
Absorption/Desorption rate constant, C_a/C_d	$59.187 \text{ s}^{-1} / 9.57 \text{ s}^{-1}$	[91, 92]
Specific heat of hydrogen gas, C_p^g	$14890 \text{ J (kg K)}^{-1}$	[92]
Specific heat of metal hydride, C_p^s	$419 \text{ J (kg K)}^{-1}$	[92]
Enthalpy of reaction, ΔH	30478 J mol^{-1}	[73]
Activation energy for absorption/desorption, E_a/E_d	$21179.6/16473 \text{ J mol}^{-1}$	[91, 92]
Porosity of metal hydride, ε	0.5	[47]
Thermal conductivity of hydrogen gas, k^g	$0.1815 \text{ W (m K)}^{-1}$	[73]
Thermal conductivity of hydrogen gas, k^s	2 W (m K)^{-1}	[73]
Molar mass of hydrogen, M^g	$2.01588 \text{ g mol}^{-1}$	[73]
Permeability of the metal hydride, K	10^{-8} m^2	[92]
Dynamic viscosity of hydrogen gas, μ	$8.4 \times 10^{-6} \text{ kg (m*s)}^{-1}$	[73]
Hydrogen-free metal density, ρ_{emp}^s	7164 kg m^{-3}	[73]
Saturated metal density, ρ_{sat}^s	7259.2 kg m^{-3}	[73]
Specific heat of (liquid) PCM, $C_p^{p,l}$	$2770 \text{ J (kg K)}^{-1}$	[92]
Specific heat of (solid) PCM, $C_p^{p,s}$	$1730 \text{ J (kg K)}^{-1}$	[93]
Thermal conductivity of (liquid) PCM, $k^{p,l}$	$0.58 \text{ W (m K)}^{-1}$	[88]
Thermal conductivity of (solid) PCM, $k^{p,s}$	$1.32 \text{ W (m K)}^{-1}$	[88]
Density of (liquid) PCM, $\rho^{p,l}$	1780 kg m^{-3}	[88]
Density of (solid) PCM, $\rho^{p,s}$	2140 kg m^{-3}	[88]
Melting temperature of PCM, T^{mel}	303 K	[88]
Range of transition temperature, ΔT^p	2 K	[88]
Latent heat of PCM, L^p	296 kJ kg^{-1}	[73]

Table 3.3 Geometrical properties of the base case

Description	Value
Inner radius of reactor, R_i	0.025 m
Inner height of reactor, H_i	0.06 m
External radius of reactor, R_e	0.038 m
External height of reactor, H_e	0.07 m
Radius of hydrogen inlet/outlet, R	0.005 m
Volume of MH bed	117.81 cm ³
Volume of PCM bed	199.74 cm ³

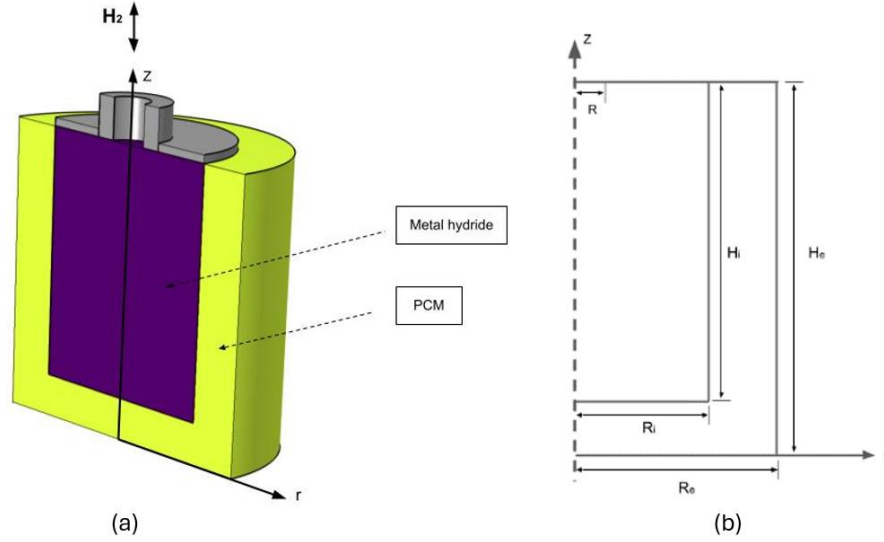


Figure 3.7 Schematic drawing of a base case: (a) cross-sectional and (b) 2D axisymmetric views

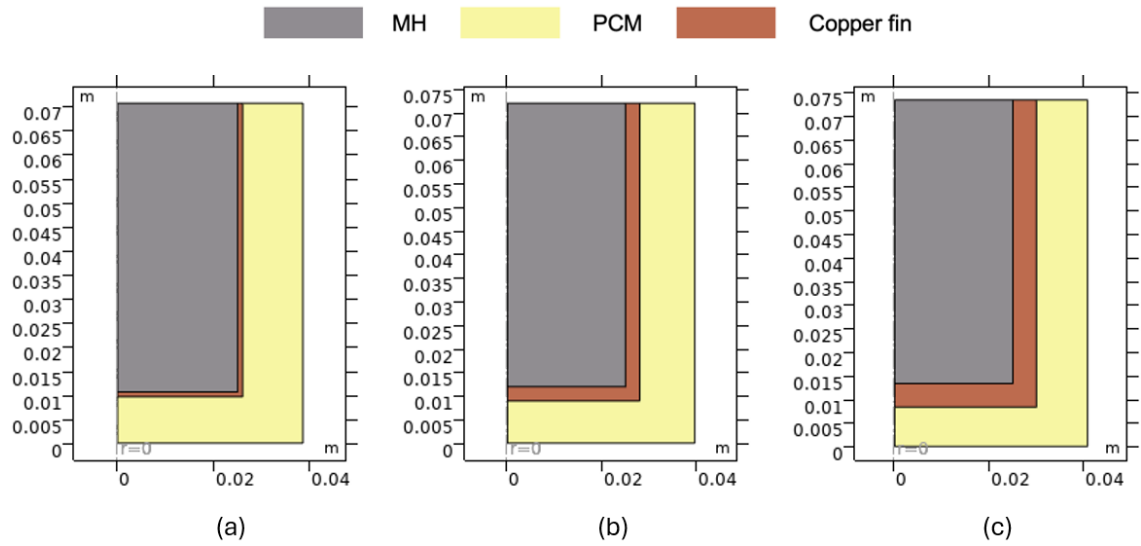


Figure 3.8 2D axisymmetric computational models showing 1 mm (a), 3 mm (b) and 5 mm (c) thicknesses of embedded copper fins between the MH and the PCM layers

3.2.2. Design #1

Once the base case was validated against already published studies, three different models have been proposed as shown in Figure 3.8. These three models are similar to the base case; however, each model includes 1 mm, 3 mm and 5 mm thicknesses of copper fins between the MH and PCM beds to analyse the effects of copper fins and their thicknesses on the hydrogen sorption reactions. For fair evaluation, the volumes of the MH and PCM beds were kept constant for the base case and the three models in Design #1.

3.2.3. Design #2 and #3

To further enhance the hydrogen sorption rates by optimising the MH-PCM reactor, a new reactor with sandwich layers of the MH and PCM beds has been proposed (Design #2) as shown in Figure 3.9(a). In this design, total 10 layers of the MH and PCM beds are axially placed. There is a hydrogen flow channel in the innermost area where hydrogen flows to and from the MH bed. Design #2 has been further optimised (Design #3) by including copper fins between each layer of MH and PCM beds as shown in Figure 3.9(b). Similar to Design #1, total volumes of MH and PCM beds in Design #2 and Design #3 were kept constant for fair evaluation of their performance. Most numerical studies of MH-PCM reactors and the proposed designs in this study were tested under adiabatic wall conditions, which assume the perfect insulation that is not appropriate for real applications. Therefore, Design #3 was further evaluated under the non-adiabatic wall conditions and under the recorded ambient temperature [94] to test its reversibility in the real-life scenario.

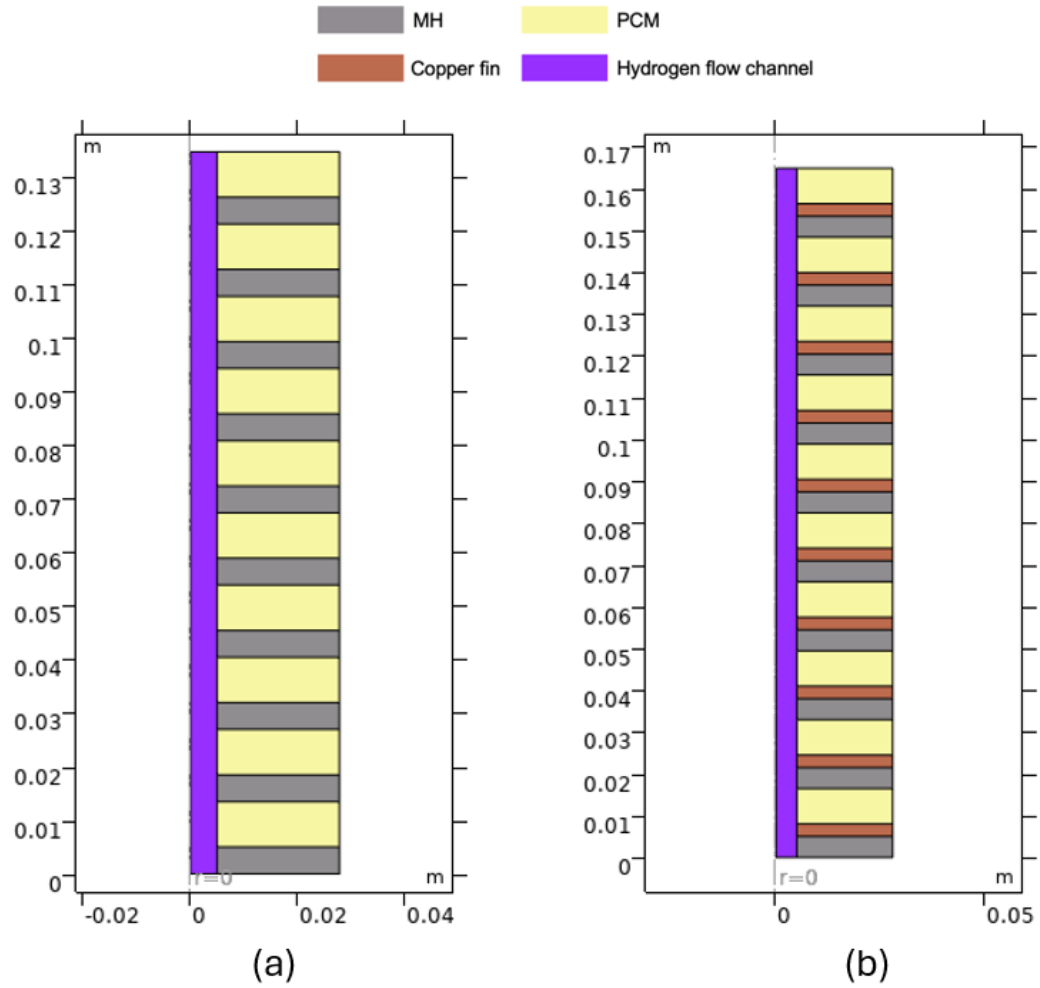


Figure 3.9 2D axisymmetric computational models of 10 sandwich layers of the MH and PCM beds, Design #2, (a) and 10 sandwich layers of the MH-Fin-PCM, Design #3 (b)

3.3. Numerical Setting

As mentioned in the section **2.1**, numerical modelling with CFD involves governing equations to describe mass and heat transfer. In this study, the governing equations are based on the following assumptions:

- Ideal hydrogen following ideal gas law [12]
- The isotropic MH [91]
- Constant and uniform porosity, permeability, and tortuosity of the MH [91]
- Local thermal equilibrium between hydrogen and the MH [95]
- Negligible radiation effects within the MH bed [95]
- Negligible convection heat transfer within the PCM [70]
- Negligible expansion of the MH and PCM beds [91]

3.3.1. Governing equations for the MH bed

Governing equations for hydrogen and the MH bed follow Eq. 1 to Eq. 13 described in the section **2.1**.

3.3.2. Governing equations for the PCM bed

Energy equations for the PCM bed is highly dependent on volumetric enthalpy and temperature. [70] With the assumption of negligible convection heat transfer due to low velocity, the thermal energy equation is expressed as follows.

$$\frac{\partial H^p}{\partial t} = \nabla \cdot (k^p \nabla T) \quad (14)$$

In Eq. 14, H^p refers to the total volumetric enthalpy and is related to sensible enthalpy and latent heat of PCM expressed as follows.

$$H(T) = h(T) + \rho^p L^p f(T) \quad (15)$$

In Eq. 15, h , L^p and f indicate the sensible heat, the latent heat and the mass fraction of PCM, respectively. L^p and f are further expressed in

$$h(T) = \int_{T_m}^T \rho^p C_p^p dT \quad (16)$$

$$f = \frac{1}{2} \frac{(1 - \theta) \rho^{p,s} - \theta \rho^{p,l}}{\rho^p} \quad (17)$$

In Eq. 16/17, $\rho^{p,s}$ and $\rho^{p,l}$ refer to the density of solid state PCM and liquid state PCM, respectively. θ is the liquid fraction of PCM expressed as follows.

$$\theta = \begin{cases} 1 & \text{if } T > T^{mel} + \frac{\Delta T^p}{2} \\ \frac{1}{1 + e^{-7(T - T^{mel})}} & \text{if } T^{mel} - \frac{\Delta T^p}{2} < T < T^{mel} + \frac{\Delta T^p}{2} \\ 0 & \text{if } T < T^{mel} - \frac{\Delta T^p}{2} \end{cases} \quad (18)$$

By substituting Eq. 15 and Eq. 16 to Eq. 14, the energy equation of the PCM bed is expressed as follows.

$$(\rho^p C_p^p) \frac{\partial T}{\partial t} = \nabla \cdot (k^p \nabla T) - \rho^p L^p \frac{\partial f}{\partial t} \quad (19)$$

3.3.3. Initial and boundary conditions

Initial conditions for the hydrogen absorption and desorption reactions slightly differ due to different thermophysical phenomena during these reactions in the MH and PCM beds.

In addition, initial conditions for the MH bed and the PCM bed are assumed uniform.

For the absorption reaction:

$$T_0 = 293 \text{ K}, P_0 = P_{eq,a(T=273 \text{ K})} = 0.069192 \text{ MPa}, \rho_0^s = \rho_{emp}^s \quad (20)$$

For the desorption reaction:

$$T_0 = 313 \text{ K}, P_0 = P_{eq,d(T=313 \text{ K})} = 0.282 \text{ MPa}, \rho_0^s = \rho_{sat}^s \quad (21)$$

The boundary conditions are as follows.

(1) Adiabatic hydrogen inlet and outlet

$$\nabla T_{in/out} \cdot \vec{n} = 0 \quad (22)$$

(2) Adiabatic symmetric wall

$$\nabla T^s \cdot \vec{n} = \nabla T^p \cdot \vec{n} = 0 \quad (23)$$

(3) Adiabatic external wall

$$\nabla T_{ext} \cdot \vec{n} = 0 \quad (24)$$

(4) Internal MH-PCM boundary wall

$$\lambda^s \nabla T^s \cdot \vec{n} = \lambda^p \nabla T^p \cdot \vec{n} \quad (25)$$

(5) Inlet and outlet boundary pressure

$$P_{in} = 1 \text{ MPa}, P_{out} = 0.1 \text{ MPa} \quad (26)$$

3.4. Results and Discussion

3.4.1. Basic MH-PCM reactor (Base Case)

Firstly, the basic design of a MH-PCM reactor as illustrated in Figure 3.7, the base case, was simulated to analyse the internal phenomena in the MH and PCM beds during the hydrogen absorption and desorption reactions.

3.4.1.1. Absorption

For the hydrogen absorption reaction, the reactor initially at 293 K and 0.1 bar was charged at the inlet pressure of 10 bar. Figure 3.10 illustrates cross-sectional contours of average temperature and reaction fraction during the hydrogen absorption reaction at various time. According to Figure 3.10(a), the entire MH bed generates excess heat in the first few seconds ($t < 100$ s), causing the average bed temperature evenly rises from the initial temperature of 293 K to 344 K. This is due to the abrupt and dominant exothermic hydrogen absorption reaction. This causes the temperature gradient between the MH and PCM beds, resulting in the convective heat transfer from the MH bed to the PCM bed. Therefore, the area near the interface between the two beds show the slightly lower and higher temperature than that of the rest of the MH bed and the PCM bed, respectively.

As the time progresses ($t < 4000$ s) more heat is transferred from the MH bed to the PCM bed, causing its average temperature to decrease and the average temperature of the PCM bed to increase. However, the average temperature in the core region of the MH bed remains high as the distance between this core region and the PCM bed causes an inefficient heat transfer between them. Eventually, the MH and PCM beds gradually reach an equilibrium temperature once significant time elapse ($t > 6000$ s).

The effects of the temperature gradient and heat transfer between the two beds can describe the behaviour of the hydrogen and PCM reactions as shown in Figure 3.10(b). In the first few seconds ($t < 100$ s), most hydrogen is absorbed in the MH bed near the interface. Similarly, most $\text{LiNO}_3 \cdot 3\text{H}_2\text{O}$ near the interface is melted and become a liquid state. As explained, the effective heat transfer near the interface during the first few seconds causes faster reaction in the MH and PCM beds near the interface. As time progresses ($t < 4000$ s), much more area in the MH and PCM beds closer to the interface react. However, reactions are still not active in the core MH region and in the PCM bed near the external wall, due to inefficient heat transfer between these areas. Once significant time elapse ($t > 6000$ s), the entire bed fully absorbs hydrogen, but the PCM bed near the external wall remains in a solid state. This indicates that the volume of the PCM bed is high enough to absorb all generated heat by the MH bed, so small portion of the PCM bed is not affected by the transferred heat from the MH bed.

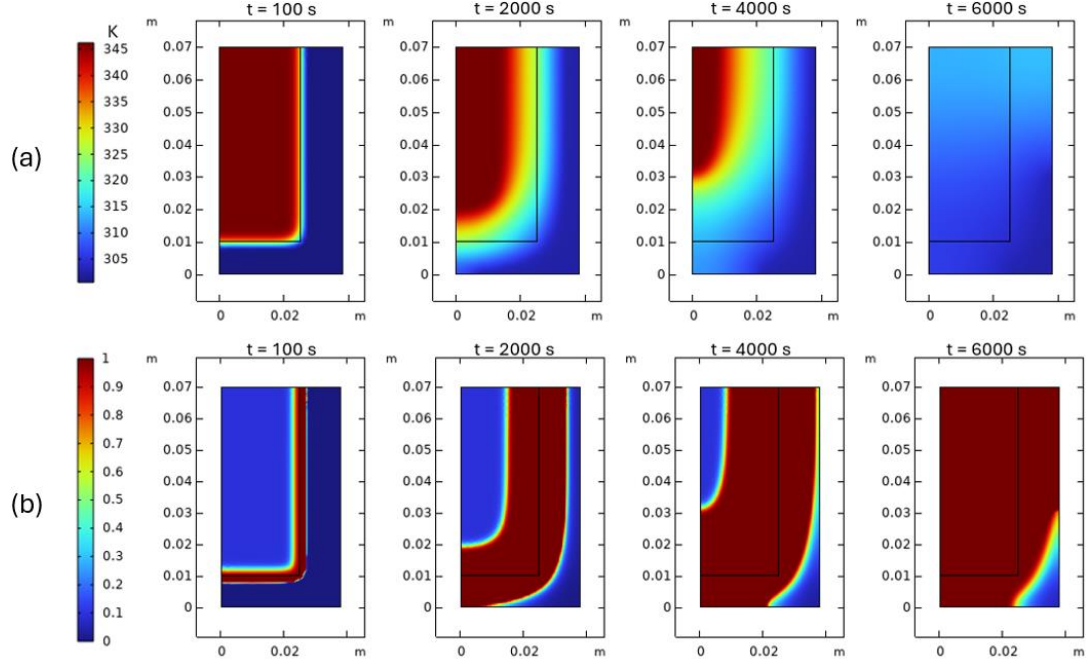


Figure 3.10 Cross-sectional contours of average temperature (a) and reaction fraction (b) during the hydrogen absorption reaction for the base case at 100 s, 2000 s, 4000 s and 6000 s

3.4.1.2. Desorption

For the hydrogen desorption reaction, the reactor initially at 313 K and 0.282 MPa was discharged at the outlet pressure of 0.1 MPa. Figure 3.11 illustrates cross-sectional contours of average temperature and reaction fraction during the hydrogen absorption reaction at various time. According to Figure 3.11 (a), the average temperature of the MH bed evenly decreases from 313 K to 289 K in the first few seconds ($t < 100$ s) due to the abrupt and dominant endothermic hydrogen desorption reaction. As the MH bed temperature decreases, it causes a temperature gradient between the MH and PCM beds,

leading an effective heat transfer from the liquid PCM bed to the MH bed near the interface. Therefore, the MH bed near the interface is slightly higher than that of the rest of the MH bed while the PCM bed near the interface is slightly lower than that of the rest of the PCM bed. As time elapse ($t < 7000$ s), heat transfer between the two beds still occurs in more areas near the interface. However, the core region of the MH bed remains the lowest average temperature due to the inefficient heat transfer between this core region and the PCM bed. Once significant time elapse ($t > 15000$ s), the two beds eventually reach an equilibrium temperature.

According to Figure 3.11 (b), only small portion of the MH bed and the PCM beds near the interface react in the first few seconds ($t < 100$ s). Near the interface, the initially liquid PCM transfers its stored latent heat to the MH bed, causing hydrogen to be desorbed and the PCM to solidify. As time elapse ($t < 7000$ s), much more area closer to the interface react as the liquid PCM keeps transferring heat to the MH bed and solidifies by transferring heat. However, due to the inefficient heat transfer between the inner core region of the MH bed and the outer PCM bed, hydrogen is still saturated in the inner core region of the MH bed while the outer PCM remains a liquid state. As significant time elapse ($t > 15000$ s), most hydrogen is absorbed while the outer PCM remains a liquid state, indicating that the volume of the PCM bed is high enough to desorb most of hydrogen in the MH bed by transferring the stored heat from the PCM bed to the MH bed.

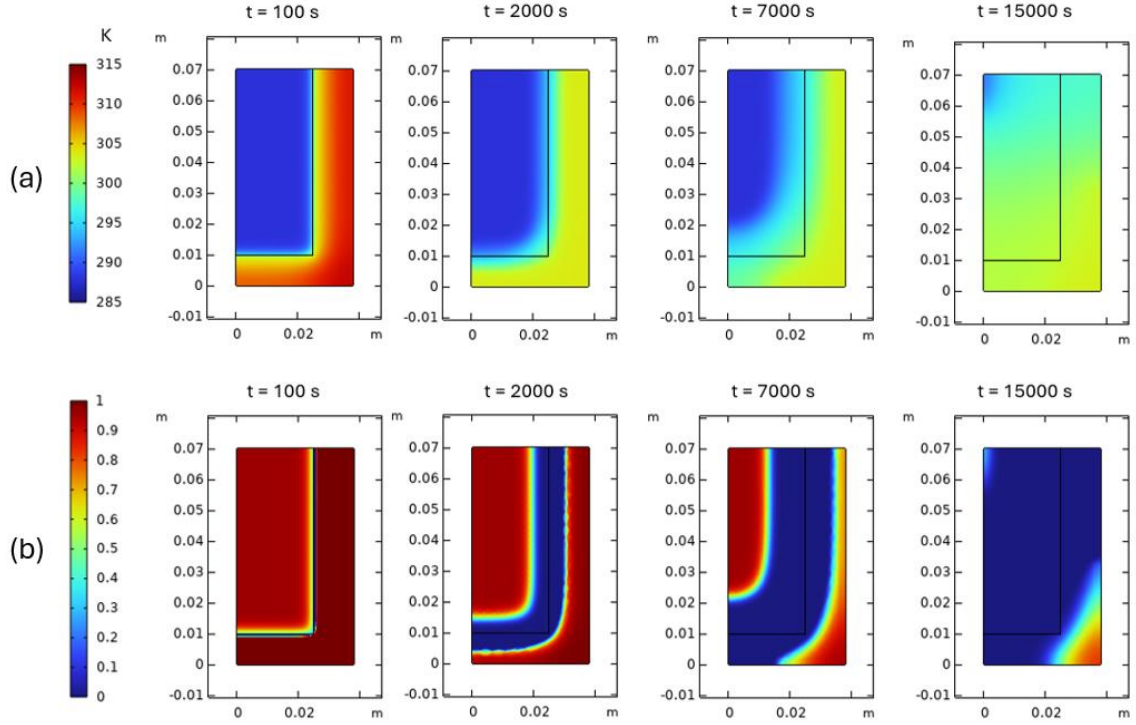


Figure 3.11 Cross-sectional contours of average temperature (a) and reaction fraction (b) during the hydrogen desorption reaction for the base case at 100 s, 2000 s, 7000 s and 15000 s

3.4.2. Optimised designs (Design #1 ~ #3)

The base case was simulated to analyse its internal phenomena during hydrogen absorption and desorption reactions. To further enhance the performance of the MH-PCM reactor, several improved designs have been proposed as introduced in the section 3.2. Their performances were evaluated based on the hydrogen reaction time and heat storage & release of the PCM bed.

3.4.2.1. Effects on the hydrogen reaction rate

Figure 3.12 and Figure 3.13 show the reacted fractions of hydrogen and the PCM during hydrogen absorption and desorption reactions for each design of a MH-PCM reactor. Table 3.4 lists improvements in the hydrogen reaction rate for Design #1 to #3, compared to the base case. From Design #1, it can be inferred that higher thickness of the embedded copper fin results in faster hydrogen reaction as higher thermal conductivity of the copper fin leads to more effective heat transfer between the MH and PCM beds. However, by comparing the hydrogen reaction time for Design #1 and #2, the hydrogen reaction time for Design #2 is significantly lower than that of Design #1, regardless of how thick the embedded copper fin in Design #1 is. For example, Design #1 with 5mm embedded copper fin recorded 3030 s and 7217 s for hydrogen absorption and desorption reactions, respectively, whereas Design #2 recorded 228 s and 629 s for hydrogen absorption and desorption, respectively. This indicates that the axial sandwich configuration of the MH and PCM beds is highly effective in terms of heat transfer between these two beds due to increased effective heat transfer surface areas. Design #3 marked slightly faster hydrogen sorption than Design #2. As Design #3 includes 10 copper fins, unlike Design #2, it still proves that copper fins aid in heat transfer between the two beds and eventually hydrogen sorption reactions.

3.4.2.2. *Effects on the heat storage/release*

Table 3.5 final liquid fraction in the PCM bed for all design cases. For the hydrogen absorption reaction, the base case recorded the highest final PCM liquid fraction, which means that the base case has the most capacity of storing heat generated by the MH bed during the hydrogen absorption reaction. By comparing the base case and Design #1, the results indicate that the higher thickness of the embedded copper fin results in a lower final liquid fraction. This indicates that as the fin thickness increases, more heat generated by the MH bed was wasted to heat up the fin itself. Design #2 recorded even lower final liquid fraction than the base case and Design #1 for the hydrogen absorption reaction. As Design #2 includes a hydrogen flow channel, some heat generated by the MH bed was wasted to the flow channel, resulting in less heat being transferred to the PCM bed. Design #3 recorded the lowest final PCM liquid fraction for the hydrogen absorption reaction as generated heat was wasted to the hydrogen flow channel and copper fins.

For the desorption reaction, the results indicate that less heat is required as the fin thickness increases. As the reaction is endothermic and the MH bed temperature abruptly decreases in the first few seconds, the relatively higher temperature of the copper fin affects the MH bed with the lower temperature. As the thickness of the copper fin increases, more initial heat in the copper fin is transferred to the MH bed, which eventually affects less heat to be transferred from the PCM bed to the MH bed. Design #2 marked the lowest final PCM liquid fraction for the desorption reaction, meaning the most heat was released from the PCM bed.

Heat initially stored in the PCM bed in Design #2 was transferred not only to the MH bed but to the hydrogen flow channel, whereas less heat was released by the PCM bed in Design #3, due to the existence of the copper fins in Design #3.

The results show that the hydrogen sorption rate and the heat storage capacity are inversely proportional to each other. As the hydrogen reaction rate of a certain design of a MH-PCM reactor is faster, it is less efficient as a heat storage medium. Suitable design of a MH-PCM reactor is required depending on the priority between the hydrogen sorption rate and the heat storage capacity.

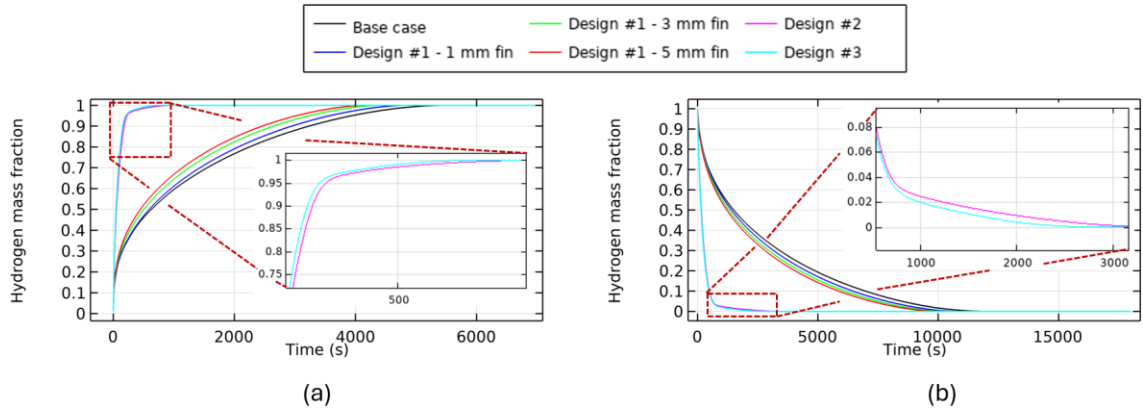


Figure 3.12 Hydrogen mass fraction during hydrogen absorption (a) and desorption reactions (b) for each improved reactor designs

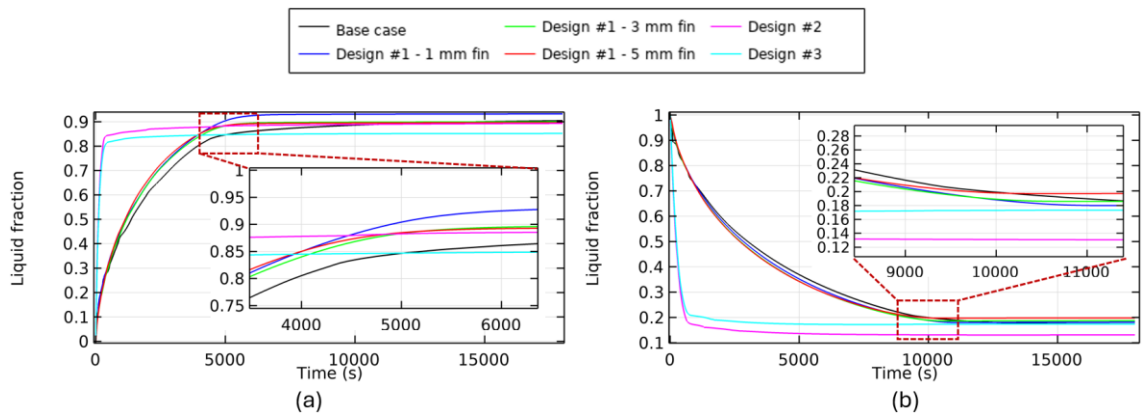


Figure 3.13 Liquid fraction during hydrogen absorption (a) and desorption (b) reactions for each improved reactor design.

3.4 RESULTS AND DISCUSSION

Table 3.4 Hydrogen reaction time during absorption and desorption reactions for all the design cases, and improvement rates in the reaction time compared to that of the base case

		Base case	Design #1 – 1 mm fin	Design #1 – 3 mm fin	Design #1 – 5 mm fin	Design #2	Design #3
ABS	Time taken to charge up to 95 %	3941 s	3579 s	3240 s	3030 s	228 s	205 s
	Improvement compared to the base case	-	9.2 %	17.8 %	23.1 %	94.3 %	94.9 %
DES	Time taken to discharge up to 5 %	8493 s	7870 s	7502 s	7217 s	629 s	606 s
	Improvement compared to the base case	-	7.3 %	11.6 %	15.0 %	92.6 %	92.9 %

Table 3.5 Final liquid fraction for all the design cases

		Base case	Design #1 – 1 mm fin	Design #1 – 3 mm fin	Design #1 – 5 mm fin	Design #2	Design #3
ABS	Final liquid fraction	0.905	0.932	0.899	0.896	0.893	0.852
DES	Final liquid fraction	0.174	0.181	0.187	0.198	0.131	0.174

3.4.3. Reversibility test for Design #3

In **Chapter 2**, it was explained that efficient heat transfer management is a key to the MHHSS performance and having heat transfer pipes with HTFs is a conventional solution. However, it requires additional resources, facilities and expenses to constantly supply HTFs to MHHSS. In the sections **3.4.1** and **3.4.2**, the use of PCM instead of conventional HTFs is investigated and it was observed that a MH-PCM reactor can operate without conventional HTFs and heat transfer pipes.

Most studies of MH-PCM reactors introduced in the section **3.1** assumes an adiabatic wall condition, which requires the perfect insulation in real-life applications that is impossible. Therefore, in this section, Design #3 is further investigated to test its applicability under a realistic condition. Its reversibility is firstly tested under an adiabatic wall condition followed by a non-adiabatic wall condition as described in sections **3.4.3.1** and **3.4.3.2**, respectively. In a non-adiabatic wall condition, the reactor wall is affected by ambient wall temperatures. For a realistic approach, ambient temperature recorded in Randwick, Sydney, New South Wales, Australia, between 05:00 and 20:00 on 01/Oct/2023, reported by Riley et al. [94] as shown in Figure 3.14. To test the reversibility, multiple absorption and desorption reactions continue back and forth. For example, during each absorption reaction, hydrogen is charged until 99% of the MH bed is saturated with hydrogen. Following that, a desorption reaction instantly occurs and stops once only 1% of the MH bed is left with saturated hydrogen.

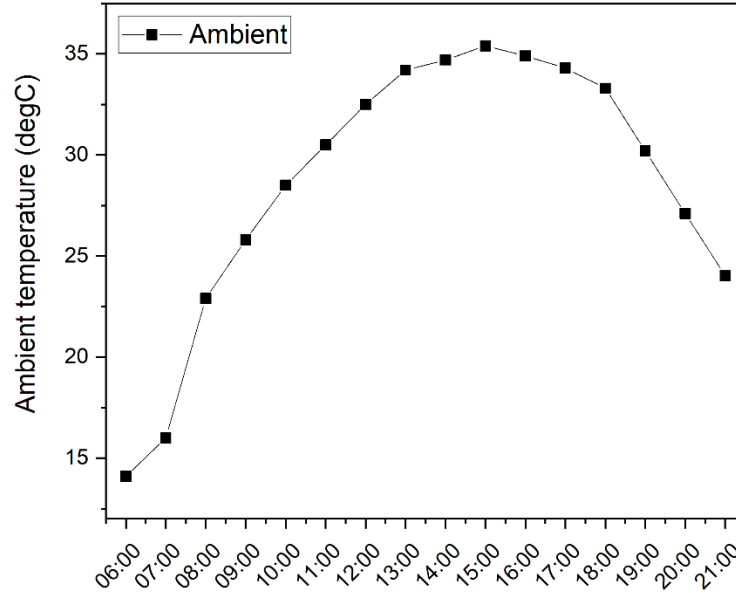


Figure 3.14 Hourly average ambient temperature recorded in Randwick, Sydney, New South Wales, Australia, on 1/Oct/2023 [94]

3.4.3.1. Ideal adiabatic wall condition

Figure 3.15 shows five continuous absorption and desorption reactions for Design #3 under an adiabatic wall condition, or a perfect insulation. Each absorption and desorption reactions take 515 s and 919 s, respectively, which make total 1434 s for a single cycle. In each absorption cycle, an abrupt exothermic hydrogen absorption reaction occurs for the first 150 s. In this period, 87% of hydrogen is charged within the MH bed and the average PCM bed temperature reaches 309.5 K, storing the latent heat from the MH bed. Since most of the exothermic absorption reaction is done after 150 s, the average MH bed temperature decreases due to relatively lower average temperature of

3.4 RESULTS AND DISCUSSION

the PCM bed. At the end of an absorption reaction when the reacted hydrogen mass fraction reaches 0.99, the PCM liquid fraction reaches 0.83, indicating 83% of the PCM bed is melted by absorbing heat generated by the MH bed.

Each desorption reaction occurs as soon as each absorption reaction is done. For each desorption reaction, the initial average MH bed and PCM bed temperatures are 307.6 K and 304.8 K, respectively. During the first 100 s ($514 \text{ s} < t < 614 \text{ s}$) of each desorption reaction, the dominant endothermic hydrogen desorption reaction makes the average MH bed temperature to decrease to 293 K. At the same time, the initial hydrogen mass fraction of 0.99 decreases to 0.6, indicating approximately 40% of the desorption reaction occurs for the first 100 s. For the next 450 s ($614 \text{ s} < t < 1064 \text{ s}$), the low average MH bed temperature reduces the desorption reaction rate, and the MH bed is more affected by the heat from the PCM. Therefore, the average MH bed temperature starts increasing while the average PCM bed temperature keeps decreasing, transferring stored heat to the MH bed. For the next 366 s ($1064 \text{ s} < t < 1430 \text{ s}$), the endothermic absorption reaction is more dominant again as 98.3% of the entire PCM bed is already solidified and there is insufficient heat to be provided to the MH bed. Consequently, it decreases both average MH and PCM bed temperatures, and marks the end of a desorption reaction.

These results prove that a MH-PCM reactor can operate multiple hydrogen absorption and desorption reactions without conventional heat transfer pipes and HTFs, which makes a MH-PCM MHHSS cost-effective and more practical. However, it is valid as long as a MH-PCM reactor is under the assumption of a perfect insulation.

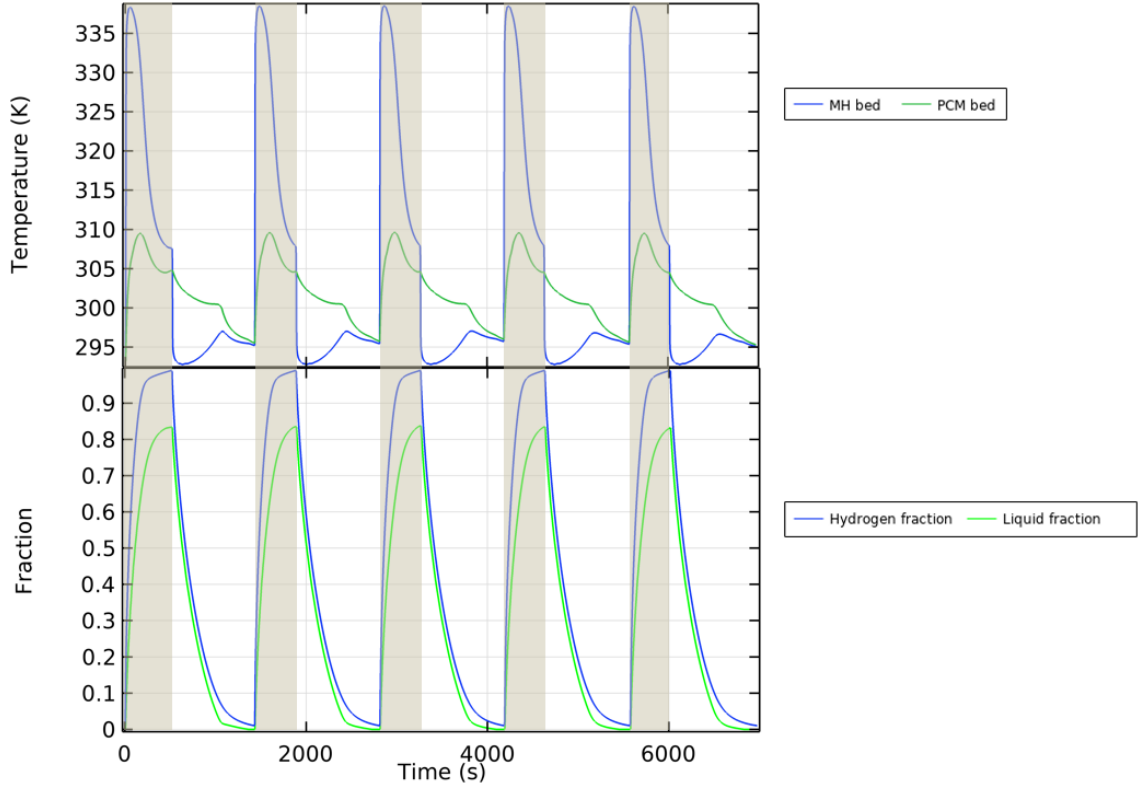


Figure 3.15 Average MH & bed temperature (top) and PCM liquid fraction & hydrogen mass fraction (bottom) during total five continuous absorption and desorption periods for design #3. Shaded and unshaded areas indicate hydrogen absorption and desorption reactions, respectively.

3.4.3.2. Non-adiabatic wall condition

For a non-adiabatic wall condition, Design #3 was assumed to be insulated with a 50 mm polyurethane layer. Having a low thermal conductivity around $0.033 \text{ W (m K)}^{-1}$, Polyurethane has been widely used as an effective insulation material. [96] As introduced, the ambient temperature was imported by recorded data as shown in Figure 3.14. [94] The recorded temperature ranges between 14°C and 35°C , which is a valid range to

examine whether an MH-PCM reactor like Design #3 can be operatable under such differences in the ambient temperature.

To test the reversibility of Design #3, each hydrogen and desorption reaction was repeated while the reacted hydrogen mass fraction ranges between 0.95 and 0.05. For example, each absorption reaction was assumed to be done when the reacted hydrogen mass fraction reaches 0.95, meaning 95% of hydrogen is saturated in the MH bed. Following that, a desorption reaction instantly starts and finishes once it reaches 0.05, meaning only 5% of hydrogen is left saturated in the MH bed. A total of 68 cycles were repeated over 14.4 hours of simulation under such conditions.

Figure 3.16 and Figure 3.17 show the change in average bed temperature along with the ambient temperature, while Figure 3.18 shows average temperature in each bed at the end of absorption and desorption reactions. From these figures, it is observed that the rise in ambient temperature for the first 9 hours ($t < 9$ h) result in the steady rise in average MH and PCM bed temperatures, where the PCM bed temperature is more affected than the MH bed temperature. Once the ambient temperature reaches its peak at 9 h ($t > 9$ h), average temperatures of both the MH and PCM beds rises abruptly during each absorption reaction. Average temperatures of both beds also eventually rise during each desorption reaction after 9 h ($t > 9$ h).

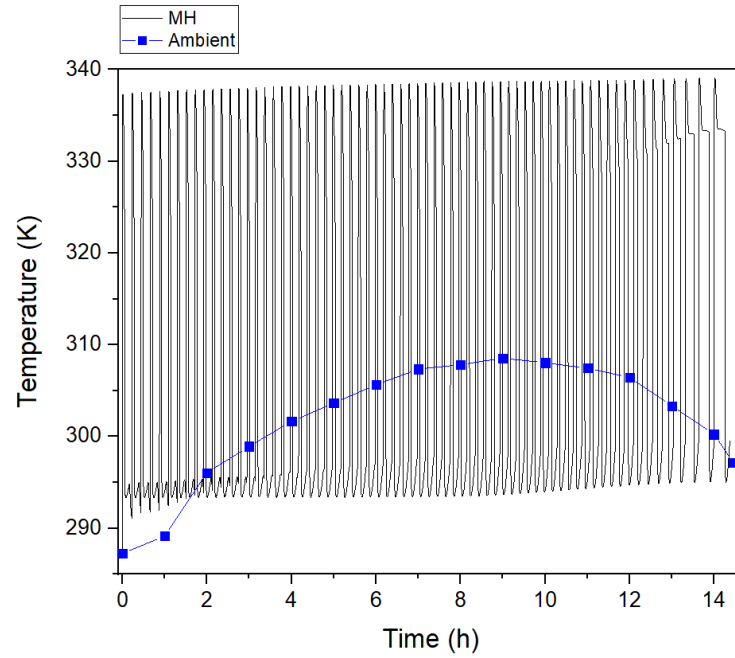


Figure 3.16 Ambient temperature and average MH bed temperature during 68 cycles of absorption and desorption reactions for Design #3

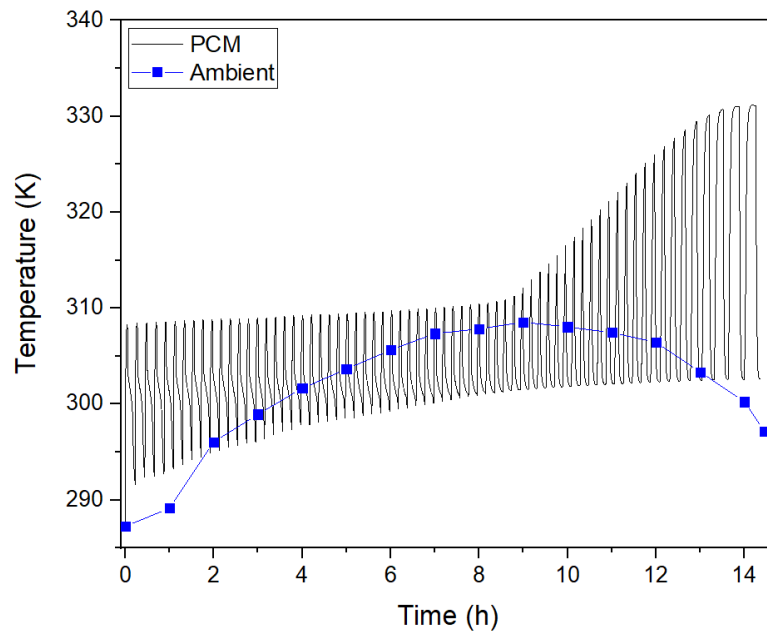


Figure 3.17 Ambient temperature and average PCM bed temperature during 68 cycles of absorption and desorption reactions for Design #3

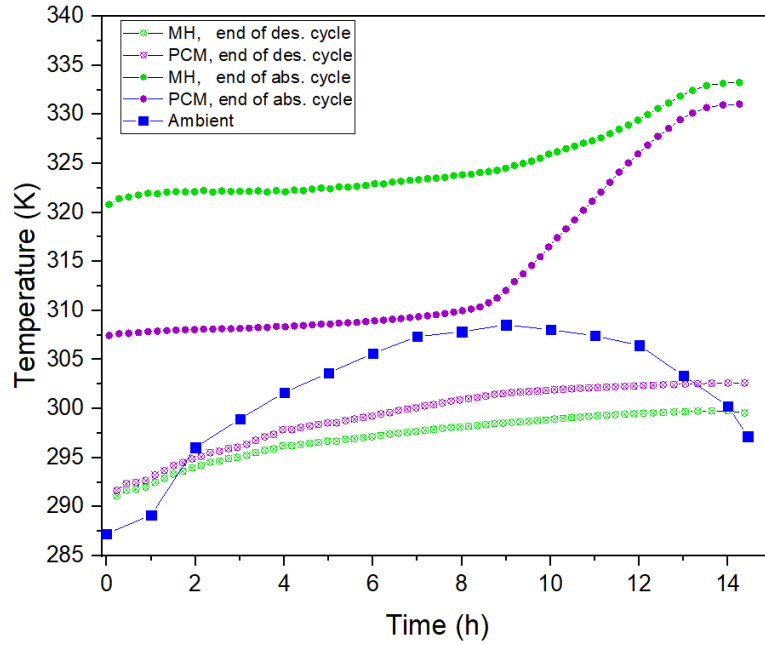


Figure 3.18 Average temperature of MH and PCM beds of Design #3 at the end of each absorption and desorption reaction along with ambient temperature during 68 cycles

Such changes in average bed temperature can be explained by changes in the PCM liquid fraction throughout the 68 cycles. Figure 3.19 and Figure 3.20 show reacted hydrogen mass fraction and PCM liquid fraction, respectively, along with the ambient temperature during 68 cycles of hydrogen absorption and desorption reactions. Figure 3.21 shows maximum and minimum hydrogen mass fraction and PCM liquid fraction throughout the cycles. From these figures, it is observed that the maximum and minimum PCM liquid fraction steadily rise during the first 8 hours ($t < 8$ h) followed by an abrupt rise in them ($t > 8$ h). For example, the maximum and minimum PCM liquid fractions in the first cycle

3.4 RESULTS AND DISCUSSION

are 0.65 and 0, respectively, whereas they are 0.97 and 0.5, respectively, in the last cycle. This indicates that the rise in the ambient temperature during the first 9 hours ($t < 9$ h) affect the PCM bed, providing additional heat to the PCM bed along with the heat generated by the MH bed during the exothermic hydrogen absorption reaction. The extra heat by the ambient and the generated heat by the MH bed are significantly higher than the heat storage capacity of the PCM bed. Therefore, the PCM bed is more vulnerable to an abrupt increase in its temperature as the ambient temperature increases.

Although each desorption reaction is endothermic and the heat in the PCM bed is transferred to the MH bed, the MH bed is not only affected by the PCM bed but also by the ambient. Therefore, less heat is transferred from the PCM bed to the MH bed during the desorption reaction, even the PCM bed is already high enough.

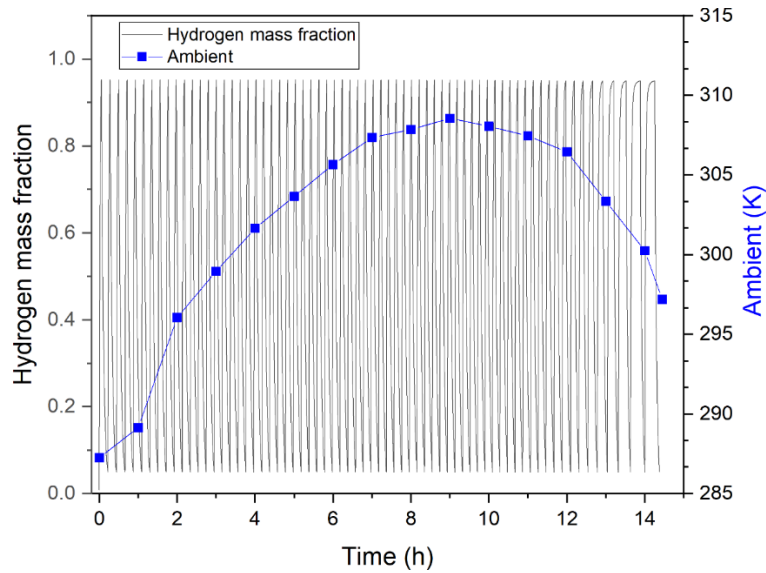


Figure 3.19 Hydrogen mass fraction along with ambient temperature during 68 cycles for Design #3

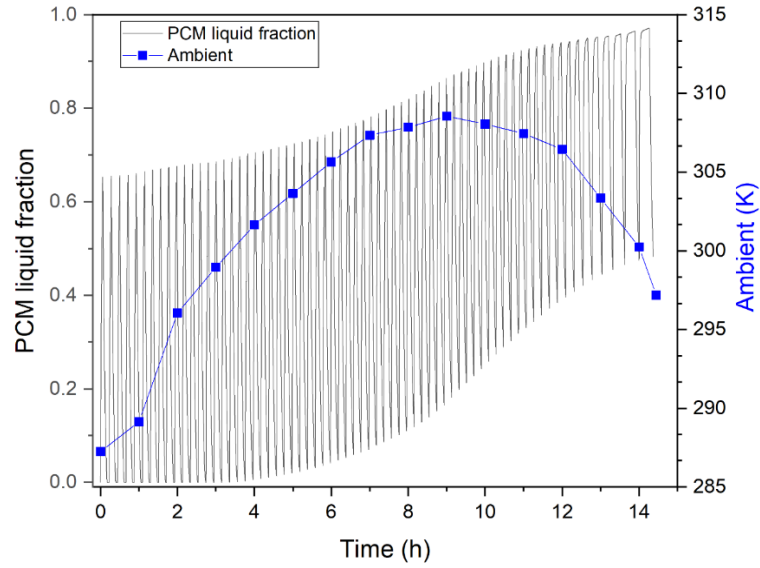


Figure 3.20 PCM liquid fraction along with ambient temperature during 68 cycles for Design #3

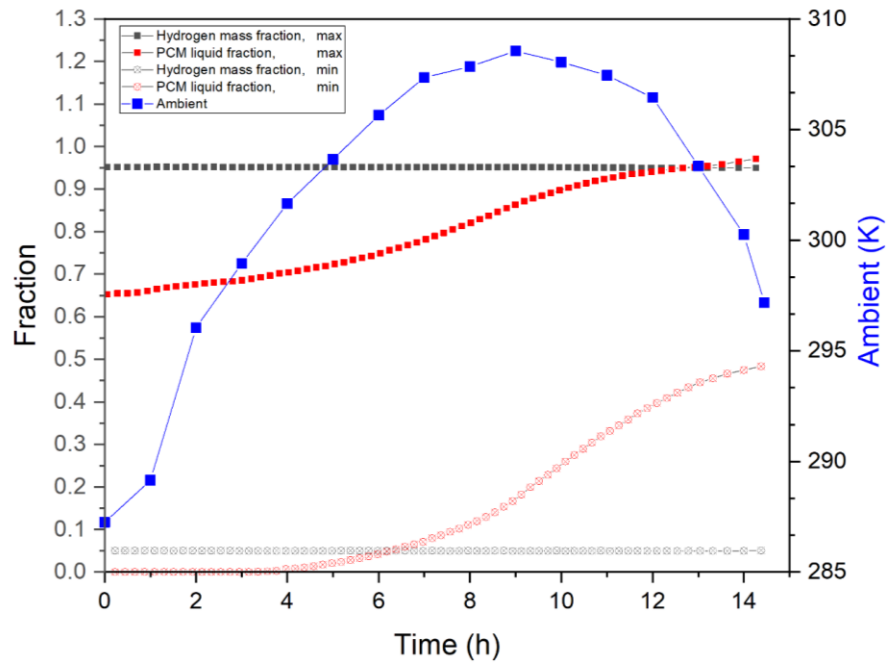


Figure 3.21 Maximum and minimum hydrogen fraction and PCM liquid fraction during each absorption and desorption cycle along with ambient temperature during 68 cycles for Design #3

As the ambient temperature rises, the overall reaction time is affected as shown in Figure 3.22. It shows a steady decrease in the desorption reaction throughout the entire cycles. For the absorption reaction time, it is almost constant during the first 9 hours ($t < 9$ h), but abruptly increases after 9 hours of the reaction ($t > 9$ h). As stated, the rise in the ambient temperature and the overall PCM bed temperature shorten the hydrogen desorption reaction, as an endothermic reaction favours higher temperatures. However, an exothermic hydrogen absorption reaction favours lower temperatures. Since the overall temperature significantly increases after 9 hours ($t > 9$ h), this results in slower hydrogen absorption reaction time.

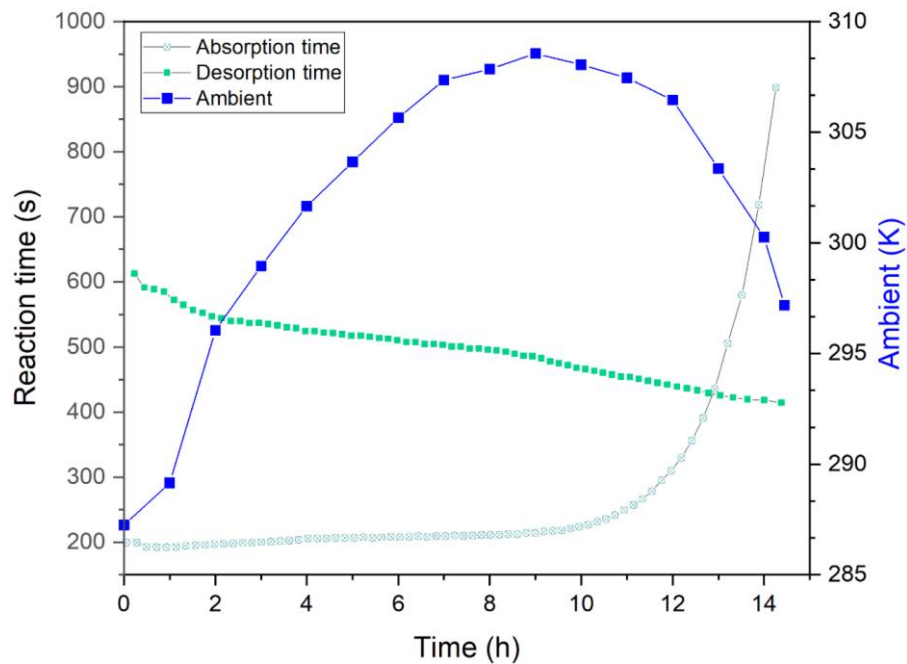


Figure 3.22 Operational time during each absorption and desorption cycle along with ambient temperature

68 cycles of absorption and desorption reactions for Design #3 show that a MH-PCM reactor can operate multiple reactions although the adiabatic wall condition is not assumed. However, it is observed that the rise in the ambient temperature can increase the hydrogen absorption reaction time. Therefore, in real-life applications, an appropriate choice of MH and PCM materials is required based on environmental conditions, such as ambient temperatures. Additionally, an effective insulation of a MH-PCM reactor is expected as better insulation will allow a MH-PCM reactor more resistant to changes in the ambient temperature.

3.5. Summary

In this study, MH-PCM reactors with various designs were developed and numerically studied to test their operation without conventional HTFs, which then would be economical and more applicable to various situations. In this study, LaNi_5 and $\text{LiNO}_3 \cdot 3\text{H}_2\text{O}$ were chosen for the MH and PCM materials, respectively.

The base case is a conventional MH-PCM reactor where the external PCM bed is surrounding the internal MH bed. With this design, typical internal heat and mass transfer phenomena during hydrogen absorption and desorption reactions were analysed. In addition, it was proven that the MH-PCM reactor can operate without conventional HTFs, although the reaction could be slower compared to a conventional MHHSS with HTFs.

Therefore, Design #1 was developed to test the effectiveness of embedded copper fins with different thicknesses between the MH and PCM beds. It was observed that a thicker copper fin results in faster hydrogen absorption and desorption reaction rates due to enhanced heat transfer between the two beds by high thermal conductivity of a copper fin. Compared to the base case, MH-PCM reactors with 1 mm, 3 mm, and 5 mm of embedded copper fins enhanced the reaction rates by 9.2%, 17.8%, and 23.1%, respectively, for the hydrogen absorption reaction and by 7.3%, 11.6%, and 15.0%, respectively, for the hydrogen desorption reaction.

To further enhance the reaction rate, Design #2 and #3 were proposed, which enhances heat transfer between the two beds by increasing heat transfer surface areas with a sandwich-shaped MH and PCM configuration. Design #2 enhanced the reaction rate by 94.3% and 92.6% for the hydrogen absorption and desorption reactions, respectively, compared to the base case. Design #3, which additionally includes 3 mm-thick copper fins between MH and PCM beds, further enhanced the reaction rate by 94.9% and 92.9% for the hydrogen absorption and desorption reactions, respectively, compared to the base case. The results also show that when the reaction rate increases, the capacity of heat storage and release by the PCM bed becomes more inefficient. Therefore, in real-life applications, an appropriate design of a MH-PCM reactor is required depending on the priority between the reaction time or heat storage performance.

Lastly, Design #3 was further tested to observe its reversibility under non-adiabatic wall conditions unlike previous numerical studies which mostly assume adiabatic wall

conditions, which is not feasible in most scenarios. Under an adiabatic wall condition, Design #3 can operate continuous hydrogen absorption and desorption reactions almost infinitely as it is not affected by an ambient temperature. However, under a non-adiabatic wall condition, Design #3 can be vulnerable to the change in ambient temperature, even though the model was assumed to be insulated with 50 mm thickness of polyurethane. As the ambient temperature increased, excess heat was provided to the PCM bed during the hydrogen absorption reaction, and the overall temperature of the PCM bed gradually increased, which eventually made the hydrogen absorption reaction slower and more than half of the PCM bed remains in a liquid state even during the hydrogen desorption reaction.

In conclusion, a MH-PCM reactor can operate without conventional HTFs, which is more economical and can be applicable to more real-life scenarios. With selections of appropriate MH and PCM materials, and with an effective insulation, a MH-PCM reactor can independently operate in any environment.

Chapter 4 MHHSS design optimisation by the integration of CFD and ML

4.1. Introduction

When it comes to industrial applications of a MHHSS, selecting its optimal design parameters and operating conditions is critical for both a manufacturer and end-user. Even slightly different design parameters and operating conditions could result in failure at meeting the engineering standards, customer requirements, or upstream and downstream specifications. In previous chapters, several advantages of CFD are discussed. However, one cannot determine optimal design and operating parameters of MHHSS with a single CFD simulation. It rather requires multiple simulations by iteratively changing parameters to determine optimal parameters, which require significant computational cost and time. However, ML-integrated CFD analysis can resolve such drawbacks. Machine learning predicts, classifies, or clusters new data after iteratively training input data based on statistical algorithms. [97–99] There are three broad types of machine learning types, such as supervised, unsupervised, and reinforcement learnings. Supervised learning trains labelled data, but unsupervised learning trains unlabelled data, finding relationships among them. [97, 98] In reinforcement learning, an agent improves a policy by interacting with environment when performing a given objective. [100]

Machine learning has also been widely applied to the hydrogen industry, including production [99, 101, 102], fuel cells [103, 104] and storage [105–114]. Ozbas et al. [99] applied various ML algorithms, such as linear regression, support vector machine (SVR) regression and decision tree regression (DTR) to predict hydrogen production concentrations from biomass. Yu et al. [101] applied artificial neural network (ANN) and accurately predicted hydrogen production from the process of steam methane reforming and pressure swing adsorption. Most ML studies on hydrogen storage focus on material-wise data, such as effects of different MH types. [105, 106, 108, 110, 112] Rahnama et al. [105] applied boosted DTR, Bayesian linear regression, neural network regression and linear regression to predict hydrogen weight percentage of various MH alloy types. Suwarno et al. [108] used multivariate, decision tree and random forest regression to predict hydrogen weight percentage and relevant heat of formation for AB₂ MH alloys. Several other studies focused on prediction of hydrogen storage performance given different reactor sizes [107, 113] and prediction of the hydrogen reaction rate at different HTF flowrate, temperature and its types. [111, 114]

Various MHHSS studies have focused on the optimization of an internal helical coil to enhance hydrogen storage performance. [6, 31, 35, 37, 38, 42, 43, 45, 52, 68, 69] However, ML-integrated CFD analysis on helical coil parameters has not been studied. Therefore, this chapter applies ML to predict the hydrogen absorption time given different coil parameters, such as axial pitch, coil radius, pipe radius, number of coil turns, and HTF velocity from various 3D transient models of MHHSS.

4.2. Method

Figure 4.1 shows the overall methodology of the current chapter. Since the current chapter discusses ML-integrated CFD analysis, there are two consecutive steps starting with CFD, followed by ML. In the CFD step, various 3D transient models were developed with different design and operating parameters of MHHSS. In this study, a total of 2559 numerical models were solved and their respective reaction time to absorb 21.6 g of hydrogen was derived. These results were then used as an input data for the ML step. The input data was pre-processed and was split into training and testing sets. Various ML models with supervised learning algorithms were developed, trained, and tested using the training and testing sets. If the models were either underfitting or overfitting, the models were optimised by hyperparameter tuning with cross-validations. Performance of each ML algorithm was evaluated by R^2 , MAE and MAPE.

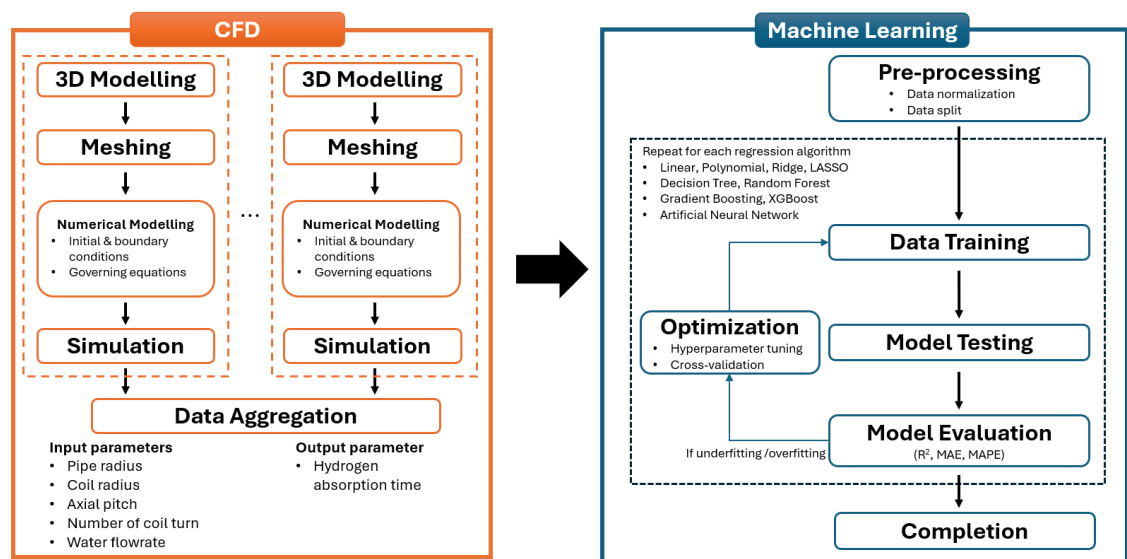


Figure 4.1 Overall methodology of the current chapter

4.2.1. Numerical model

4.2.1.1. Design

As stated, 2559 3D models were developed, and each model varies different internal helical coil design parameters while the dimensions of the external reactor remain constant. Figure 4.2 shows a typical helical coil design with different parameter names, such as axial pitch, pipe diameter, coil diameter, and the number of coil turns. Figure 4.3 illustrates three examples of MHHSS designs with internal helical coil design parameters. In addition to the design parameters, the effects of different HTF velocity were also considered. Dimensions of the external reactor and the range of internal helical coil parameters with HTF velocity are listed in Table 4.1. With such different design and operating parameters, 2559 CFD models were numerically solved and their respective reaction time to absorb 21.6 g of hydrogen were collected as shown in

Table 4.2.

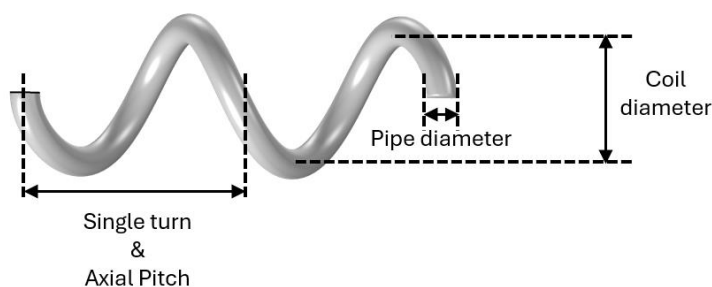


Figure 4.2 A helical coil with parameter names

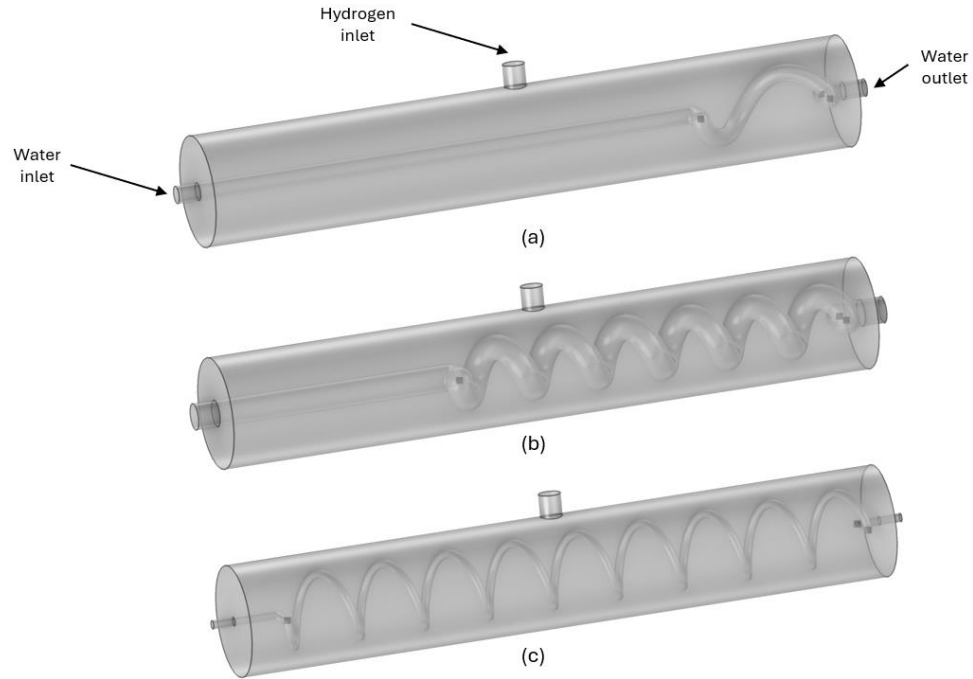


Figure 4.3 3D models of MH hydrogen storage reactors with different internal helical coil dimensions: 1 coil turn, 60 mm axial pitch, 12 mm coil radius and 4 mm coil pipe radius (a), 6 coil turns, 30 mm axial pitch, 10 mm coil radius and 6 mm coil pipe radius (b), 9 coil turns, 30 mm axial pitch, 15 mm coil radius and 2 mm coil pipe radius (c)

Table 4.1 Design parameters range for the MH hydrogen storage reactor with the internal helical coil for machine learning analysis

Description	Value (range)
Reactor radius	25 mm
Reactor height	300 mm
Hydrogen inlet radius	5 mm
Hydrogen inlet height	20 mm
Coil pipe radius	2 mm ~ 6 mm
Coil radius	10 mm ~ 15 mm
Coil axial pitch	20 mm ~ 60 mm
Number of coil turn	1 ~ 10
Heat transfer fluid (water) velocity within the coil	1.5 ~ 5.0 m/s

Table 4.2 A sample dataset for machine learning analysis

Data number	Axial pitch (mm)	Coil pipe radius (mm)	Coil radius (mm)	Number of coil turn	Heat transfer fluid velocity (m/s)	Hydrogen absorption time (s)
1	20	2	10	1	1.5	971.18
2	20	2	10	1	2.375	950.95
3	20	2	10	1	3.25	943.66
4	20	2	10	1	4.125	938.59
5	20	2	10	1	5.0	935.70
6	20	2	10	2	1.5	935.71
7	20	2	10	2	2.375	874.29
.
.
.
2598	60	6	15	4	4.125	708.39
2599	60	6	15	4	5.0	706.63

4.2.1.2. Governing equations

Governing equations for hydrogen and the MH bed follow Eq. 1 to Eq. 13 described in the section 2.1.

4.2.1.3. Initial and boundary conditions

Initial conditions for the hydrogen absorption reaction follow Eq. 20. Hydrogen inlet pressure, P_{in} , is 1 MPa. The external reactor wall and coil walls are assumed to be nonslip, and the reactor is assumed to be surrounded by water as a cooling medium. Therefore, the convective boundary condition is applied to the walls as shown in Eq. 27.

$$-k^{eff} \frac{\partial T}{\partial \vec{n}} = h(T - T_{ext}) \quad (27)$$

4.2.2. Machine learning analysis

4.2.2.1. Algorithms

ML was applied in this study to predict the hydrogen absorption time of MHHSS with the internal helical coil with different design and operating parameters. As per the nature of the ML theory, coil design and operating parameters are independent variables, whereas the hydrogen absorption time is the dependent variable. As shown in

Table 4.2, the input data includes labelled data, which makes the supervised learning algorithm is the optimal choice in this study. Therefore, linear, polynomial, Ridge, Least Absolute Shrinkage and Selection Operator (LASSO), SVR, Decision Tree, Random Forest, Gradient Boosting, XGBoost, and ANN are applied in this study.

Linear regression finds a linear relationship between independent and dependent variables using a least-squared method, as shown in Eq. 28 where β_0 is the intercept, $\beta_{1...n}$ are the slope for each dependent variable, and $x_{1...n}$ are independent variables. [115]

$$y = \beta_0 + \beta_1 x_1 + \beta_2 x_2 + \cdots + \beta_n x_n \quad (28)$$

Unlike linear regression, polynomial regression finds a non-linear relationship, as shown in Eq. 29 where β_0 is the intercept, $\beta_{1...n}$ and $\gamma_{11...nm}$ are regression coefficients, and $x_{1...n}$ are independent variables,. [111]

$$y = \beta_0 + \beta_1 x_1 + \beta_2 x_2 + \cdots + \beta_n x_n + \gamma_{11} x_1^2 + \gamma_{22} x_2^2 + \cdots + \gamma_{nn} x_n^2 \\ + \gamma_{12} x_1 x_2 + \cdots + \gamma_{ij} x_i x_j + \cdots + \gamma_{nm} x_n^m \quad (29)$$

The ordinary least square (OLS) method is applied to both linear and polynomial regression, and it minimises the squared loss as follows, where y_i is the actual data value. [116]

$$\min_{\beta} \left[\sum_{i=1}^n \left(y_i - \beta_0 - \sum_{j=1}^p \beta_j x_{ij} \right)^2 \right] \quad (30)$$

However, multicollinearity of data affect the accuracy of variance of the estimate β_j in OLS. This issue can be addressed by introducing training errors in regularization methods, such as ridge and LASSO. [116] As shown in Eq. 31 and Eq. 32, Ridge and LASSO regularization penalises the sum of the squared coefficients and the absolute sum of the coefficients, respectively. [117]

$$\min_{\beta} \left[\sum_{i=1}^n \left(y_i - \beta_0 - \sum_{j=1}^p \beta_j x_{ij} \right)^2 + \lambda \sum_{j=1}^p \beta_j^2 \right] \quad (31)$$

$$\min_{\beta} \left[\sum_{i=1}^n \left(y_i - \beta_0 - \sum_{j=1}^p \beta_j x_{ij} \right)^2 + \lambda \sum_{j=1}^p |\beta_j| \right] \quad (32)$$

The Support Vector Regression (SVR) algorithm tries to minimise an error in prediction while fitting as much data as possible within a margin of error. [118] In the following standard SVR approximation equation, $\kappa(x_i, x)$ is the kernel function, and α_i^* and α_i are Lagrange multipliers. [119]

$$y = \sum_{i=1}^n (\alpha_i^* - \alpha_i) \kappa(x_i, x) + b \quad (33)$$

Decision tree algorithms recursively split data into binary subsets, and each tree comprises a root node, internal nodes, and leaf nodes. [120] Random Forest algorithms use a bagging method, which processes multiple decision trees with randomly split input data, and averages results for prediction. [121] Gradient boosting algorithms eventually form strong learners by iteratively combining weak learners while reducing residual errors of previous models. [121] XGBoost algorithms is an improved version of gradient boosting algorithms with reduced computational complexity. [121] Inspired by the human brain process, artificial neural networks include input, hidden, and output layers with nodes in each layer. [122]

4.2.2.2. *Model development and evaluation*

CFD simulation results were combined, followed by pre-processing of the input data. 80% of the input data was split into training sets, whereas the remaining 20% was split into testing sets. Additionally, the input data was normalised using Z-score for a better computation by machine learning. Its equation is as follows, where x is a sample data, μ is the mean of the data, and σ is the standard deviation of the data.

$$z = \frac{x - \mu}{\sigma} \quad (34)$$

Scikit-learn and TensorFlow, popular open-source machine learning libraries, were used to train and test ML models. Default parameters were applied for initial model development. Several evaluation metrics, such as R^2 , Mean Absolute Error (MAE), and Mean Absolute Percentage Error (MAPE) were used to evaluate performance of each model. Their mathematical formulae are shown below. [111]

$$R^2 = 1 - \frac{\sum_{i=1}^n (y_{predicted,i} - y_{actual,i})^2}{\sum_{i=1}^n (y_{predicted,i} - y_{mean})^2} \quad (35)$$

$$MAE = \frac{1}{n} \sum_{i=1}^n |y_{predicted,i} - y_{actual,i}| \quad (36)$$

$$MAPE = \frac{1}{n} \sum_{i=1}^n \left| \frac{y_{predicted,i} - y_{actual,i}}{y_{actual,i}} \right| \quad (37)$$

To avoid underfitting or overfitting of the models, they were optimised by tuning hyperparameters with 10-fold cross-validation. The difference between the R^2 of training and testing datasets was kept less than 0.01 to ensure the model was not overfitting.

4.3. Results and Discussion

4.3.1. Effects of coil design parameters

2559 3D models of MHHSS with different internal helical coil parameters were numerically solved and their results were collected as shown in Table 4.2. Before the data was processed with ML analysis, the effects of those various internal helical coil parameters on the hydrogen absorption time were firstly analysed.

4.3 RESULTS AND DISCUSSION

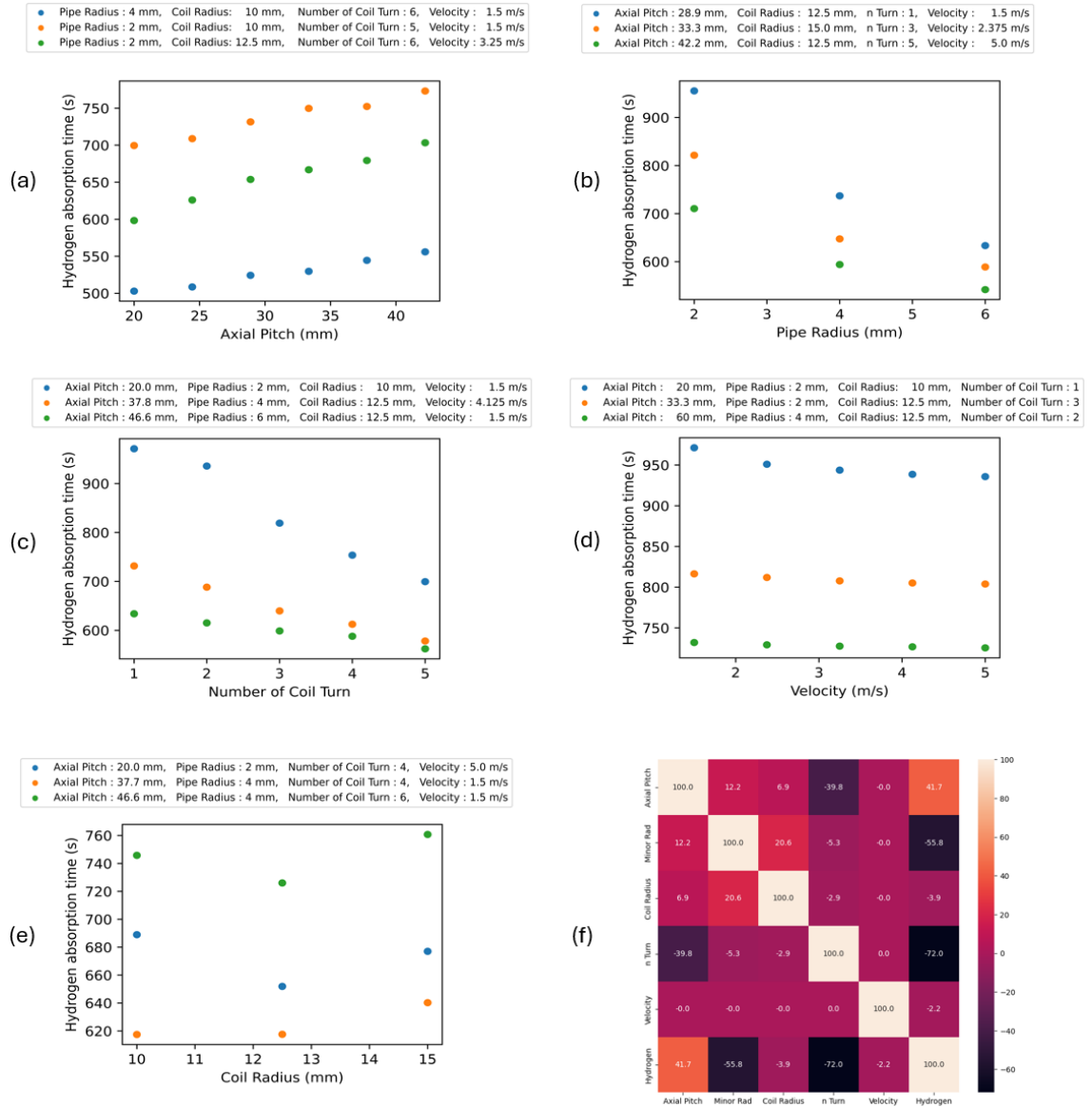


Figure 4.4 Relationship between the hydrogen absorption time and coil design parameters – axial pitch (a), pipe radius (b), number of coil turn (c), velocity of water (d) and coil radius (e), and a correlation heatmap between variables (f)

4.3 RESULTS AND DISCUSSION

Figure 4.4 shows relationships between the hydrogen absorption time to absorb 21.6 g of hydrogen and various internal coil parameters. According to Figure 4.4(a), there is a positive correlation between the axial pitch of the coil and the hydrogen absorption time, as the higher axial pitch results in less effective heat transfer surface area, causing less efficient hydrogen absorption reaction. However, other coil parameters have negative correlation to the hydrogen absorption time, as shown in Figure 4.4(b)~ Figure 4.4(e). Higher values of these parameters result in increased heat transfer surface area, causing a faster hydrogen absorption reaction. Similarly, higher HTF velocity enhances more effective convective heat transfer between the coil and the MH bed, leading to faster hydrogen absorption reaction.

Figure 4.5 illustrates more intuitively how these different coil parameters affect the hydrogen absorption time. It shows cross-sectional contours of temperature and reacted hydrogen mass fraction at three different time for four different samples (Sample 1 ~ 4). The hydrogen absorption time for Sample 1 to 4 are 556 s, 698 s, and 976 s, respectively. Sample 1 has the most overall advantageous coil parameters, followed by Sample 2 and Sample 3, where Sample 4 has the most overall disadvantageous coil parameters. For example, Sample 1 has low axial pitch, high pipe radius, high coil radius, more coil turns and high HTF velocity, whereas Sample 4 has high axial pitch, low pipe radius, low coil radius, less coil turns and low HTF velocity. Wider areas of lower temperatures near the coil of Sample 1 in Figure 4.5 show such advantageous coil parameters resulted in effective heat transfer between HTF and the MH bed. However, most areas are in high temperatures even at 380 s for Sample 4, indicating there was inefficient heat transfer between HTF and the MH bed. As more hydrogen absorption reaction is derived by

4.3 RESULTS AND DISCUSSION

relatively lower temperature, thus the lower equilibrium pressure, the hydrogen mass fraction contour in Figure 4.5 also illustrates similar phenomena. For example, most areas of Sample 1 fully absorbed hydrogen at 380 s, whereas most areas are free of hydrogen for Sample 4, due to ineffective coil parameters.

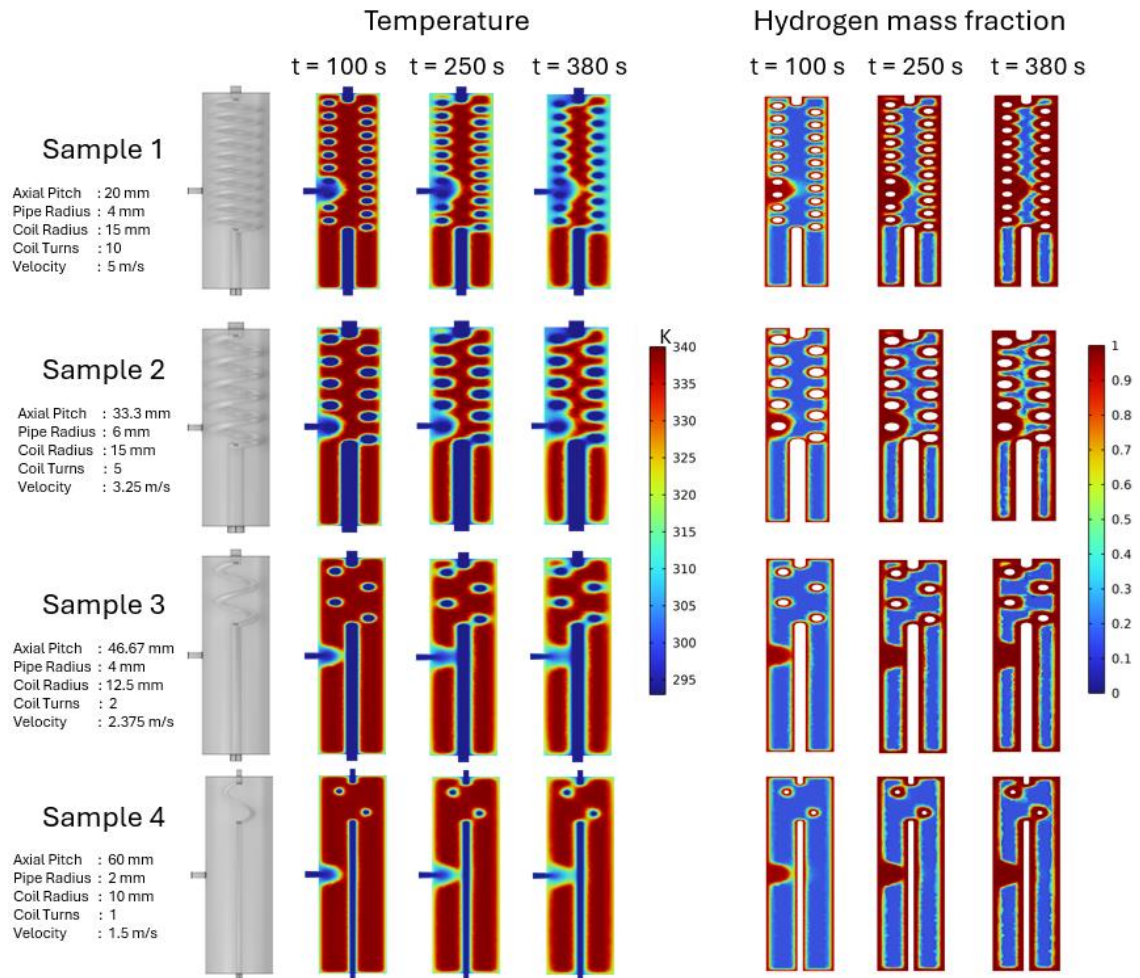


Figure 4.5 Cross-sectional contours of temperature and hydrogen mass fraction at 100 s, 250 s, and 380 s for four sampled cases with different parameters

4.3.2. Machine learning analysis

In the previous section, relationship between coil parameters and the hydrogen absorption time was studied. However, this does not predict an approximate hydrogen absorption time given certain values of coil parameters. On the other hand, machine learning models can predict the hydrogen absorption time after carefully train and tune them. Machine learning models from Scikit-learn and TensorFlow libraries were used to train and test 2559 CFD simulation results. These ML models were optimised by hyperparameter tuning with 10-fold cross validation to avoid overfitting. Lastly, the model performance was evaluated by metrics such as R^2 , MAE, and MAPE.

Figure 4.6, Figure 4.7, and Figure 4.8 show R^2 , MAE, and MAPE, respectively, of each ML model used in this study. All ML models achieved R^2 higher than 0.9, meaning that more than 90% of the variance in coil design parameters and hydrogen absorption time can be explained by these ML models. In addition, the difference between train sets of R^2 and test sets of R^2 is less than 0.01 in each model and the models are not overfitting. Figure 4.6 shows that polynomial, Ridge, and LASSO regression models, which are classic regression models, slightly outperform other tree-based models. However, the linear regression model, which is simple and does not have hyperparameters to be tuned, recorded a relatively lower R^2 .

4.3 RESULTS AND DISCUSSION

MAE and MAPE in Figure 4.7 and Figure 4.8 also show the similar trend. MAE of polynomial, Ridge, and LASSO models are comparably lower. For example, these models recorded 10 s of MAE, whereas other models recorded less than 40 seconds of MAE. The MAE values tell that all the ML models in this study can predict the hydrogen absorption time within 40 seconds of error. However, MAE does not interpret relevant terms to actual values, so it alone can be ambiguous in evaluating model performance. On the other hand, MAPE evaluates a relative error to actual values, as shown in Figure 4.8. This figure shows that the prediction of the hydrogen absorption time by the ML models in this study has an error within 5% compared to actual values. Even polynomial, Ridge and LASSO models can predict within 2% of error. Considering that the actual range of the hydrogen absorption time is between 400 to 1000 seconds, such MAE and MAPE prove that the ML models perform very well.

Figure 4.6, Figure 4.7, and Figure 4.8 show that classical regression models generally outperform tree-based models. Classical regression models, such as Ridge and LASSO, reduces overfitting of models by handling collinearity with regularization terms. However, noise in the data makes tree-based models prone to capturing them. Additionally, tree-based models can overcomplicate relationships, whereas classic regression models perform better with relatively simple relationships in input datasets. Yet, evaluation metrics suggest that the ML models in this study are effective in predicting the hydrogen absorption time.

4.3 RESULTS AND DISCUSSION

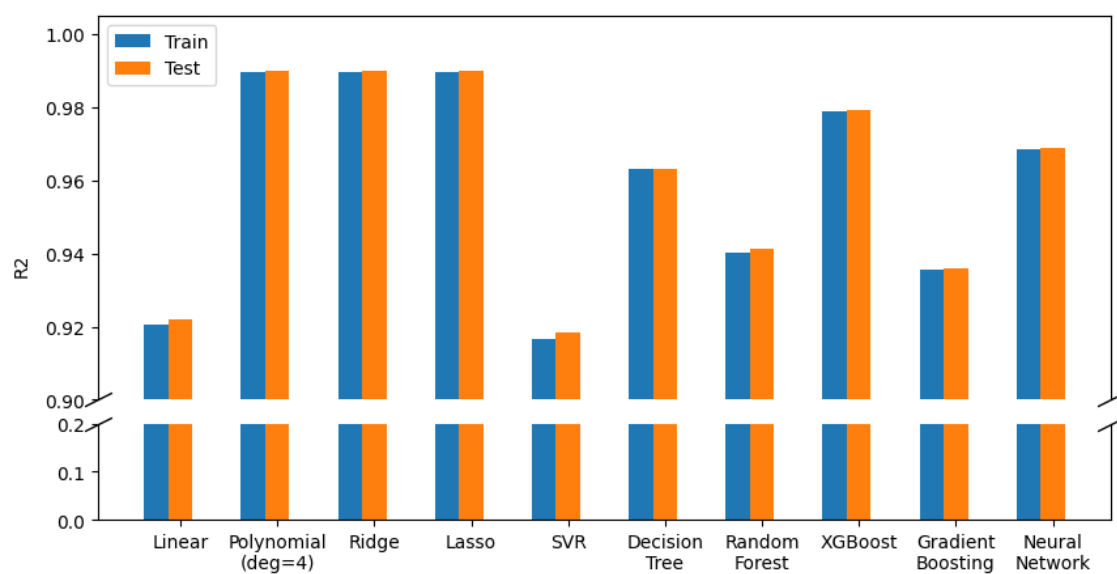


Figure 4.6 R^2 for different regression models to predict hydrogen absorption time

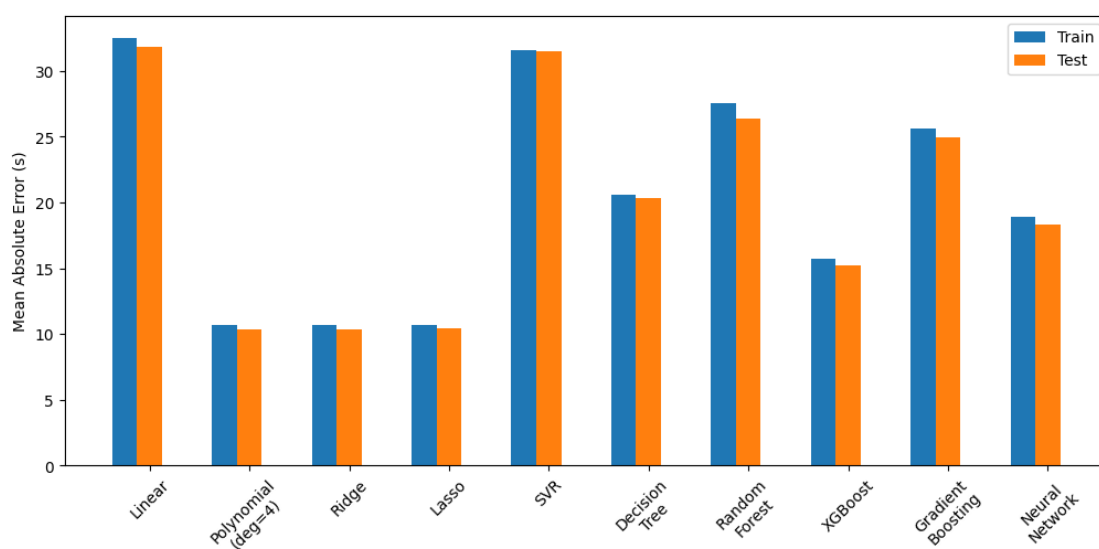


Figure 4.7 MAE for different regression models to predict hydrogen absorption time

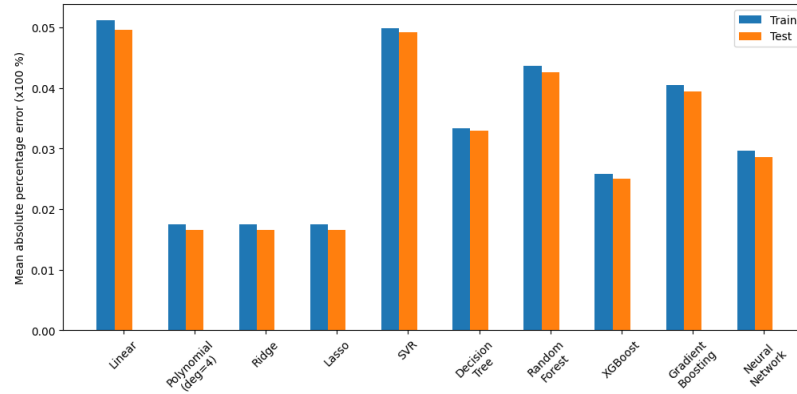


Figure 4.8 MAPE for different regression models to predict hydrogen absorption time

4.4. Summary

CFD simulations are well-known for its cost-effectiveness and applicability to design optimization as less time is required than actual experiments. However, a single CFD simulation cannot predict unseen data. Therefore, CFD and ML were integrated to study the prediction of the hydrogen absorption time given various coil parameters in MHHSS, where LaNi_5 and water were chosen as MH and HTF, respectively. Various three-dimensional CFD models were developed, and their hydrogen absorption time was numerically solved. Linear, polynomial, Ridge, LASSO, Support Vector Regression, Decision Tree, Random Forest, Gradient Boosting, XGBoost, and Artificial Neural Network models were used to predict the hydrogen absorption time given different coil parameters, such as axial pitch, pipe radius, coil radius, coil turn number, and heat transfer fluid velocity. This study suggests these conclusions.

- Lower axial pitch, higher pipe radius, higher coil radius, more number of coil turns and higher HTF velocity reduces the hydrogen absorption reaction time, due to enhanced heat transfer surface area and more convective heat transfer.
- The evaluation metrics for all ML models in this study recorded R^2 higher than 0.9, MAE less than 30 seconds, and MAPE less than 5%. This suggests that the ML models are effective in predicting the hydrogen absorption time given different coil parameters.
- Classical regression models, such as polynomial, Ridge and LASSO, outperform tree-based models or ANN, with 0.99 R^2 , 10 seconds of MAE and 1.7% of MAPE.
- Integration of CFD and ML can be effective in industry applications to predict design or operation requirements as the nature of CFD and ML allows less cost and time.

Chapter 5 Conclusion and Future Perspectives

Hydrogen is the key to the decarbonisation and to reach the green future. Therefore, the importance of not only hydrogen production but hydrogen storage has been highlighted. MHHSS is a promising hydrogen storage method with moderate operating temperature and pressure with higher storage density. However, to offset disadvantages of MHHSS, such as low gravimetric capacity and slower kinetics, design optimisation of MHHSS has been widely studied, both experimentally and numerically. Throughout this thesis, effectiveness of CFD with ML on optimisation of MHHSS is thoroughly discussed. In **Chapter 3**, the numerical study of MHHSS with PCM is discussed, and several improved designs are proposed. This chapter proves that the improved designs enhance the hydrogen sorption reaction and its potential applications as an independent system without conventional HTFs. In **Chapter 4**, integration of CFD and ML is discussed, and it showcases effectiveness in predicting design or operating requirements.

Due to the nature of cost-effectiveness and a robust process, CFD will continue to be applied to the design optimisation of MHHSS. However, CFD analysis often entails simplified or neglected assumptions, as the CFD simulation cannot implement perfect conditions. For example, the real operation of MHHSS entails MH expansion and contraction, which eventually results in deformation of MH and excess of local stresses on a reactor itself. Therefore, in the future study, a material-wise study with Finite Element Analysis (FEA) should be considered in numerical studies of MHHSS. FEA is a

5 CONCLUSION AND FUTURE PERSPECTIVES

computational prediction of an object's behaviour, such as strain and stress, based on Finite Element Method (FEM), which divides the model into smaller elements and solves differential equations upon each element. [123] CFD-FEA analysis of MHHSS will enable more realistic numerical studies of MHHSS, such as the choice of appropriate MH and reactor materials, as well as the physical impact on MHHSS during its operation.

Once an appropriate design and selections of MH and reactor materials are determined by CFD-FEA analysis, the studied MHHSS can be built and experimentally studied to further prove its real-life applications. This optimised MHHSS will operate fast and more durable due to enhanced design and appropriate selections of materials.

REFERENCES

1. Durbin, D.J., Malardier-Jugroot, C.: Review of hydrogen storage techniques for on board vehicle applications, (2013)
2. Zhang, Y.H., Jia, Z.C., Yuan, Z.M., Yang, T., Qi, Y., Zhao, D.L.: Development and Application of Hydrogen Storage, (2015)
3. Abe, J.O., Popoola, A.P.I., Ajenifuja, E., Popoola, O.M.: Hydrogen energy, economy and storage: Review and recommendation, (2019)
4. Prachi R., P., Mahesh M., W., Aneesh C., G.: A Review on Solid State Hydrogen Storage Material. *Advances in Energy and Power*. 4, 11–22 (2016). <https://doi.org/10.13189/aep.2016.040202>
5. Hwang, H.T., Varma, A.: Hydrogen storage for fuel cell vehicles, (2014)
6. Nguyen, H.Q., Shabani, B.: Review of metal hydride hydrogen storage thermal management for use in the fuel cell systems, (2021)
7. Suda, S., Kobayashi, N., Yoshida, K.: REACTION KINETICS OF METAL HYDRIDES AND THEIR MIXTURES*. (1980)
8. Mayer, U., Groll, M., Supper, W.: HEAT AND MASS TRANSFER IN METAL HYDRIDE REACTION BEDS: EXPERIMENTAL AND THEORETICAL RESULTS*. (1987)
9. Supper, W., Groll, M., Mayer, U.: REACTION KINETICS IN METAL HYDRIDE REACTION BEDS WITH IMPROVED HEAT AND MASS TRANSFER*. (1984)

10. Nasrallah, S. Ben, Jemni, A.: HEAT AND MASS TRANSFER MODELS IN METAL-HYDROGEN REACTOR.
11. Jemni, A., Nasrallah, S. Ben: CP dP E, h H Hss H/M STUDY OF TWO-DIMENSIONAL HEAT AND MASS TRANSFER DURING ABSORPTION IN A METAL-HYDROGEN REACTOR. (1995)
12. Jemni, A., Nasrallah, S. Ben: STUDY OF TWO-DIMENSIONAL HEAT AND MASS TRANSFER DURING DESORPTION IN A METAL-HYDROGEN REACTOR. (1995)
13. Jemni, A., Sassi, \, Nasrallah, B., Lamloumi, J.: Experimental and theoretical study of a metalDhydrogen reactor.
14. Dhaou, H., Askri, F., Ben Salah, M., Jemni, A., Ben Nasrallah, S., Lamloumi, J.: Measurement and modelling of kinetics of hydrogen sorption by LaNi₅ and two related pseudobinary compounds. *Int J Hydrogen Energy*. 32, 576–587 (2007).
<https://doi.org/10.1016/j.ijhydene.2006.07.001>
15. Kumar Phate, A., Prakash Maiya, M., Murthy, S.S.: Simulation of transient heat and mass transfer during hydrogen sorption in cylindrical metal hydride beds. *Int J Hydrogen Energy*. 32, 1969–1981 (2007).
<https://doi.org/10.1016/j.ijhydene.2006.09.020>
16. Askri, F., Jemni, A., Ben Nasrallah, S.: Dynamic behavior of metal-hydrogen reactor during hydriding process. *Int J Hydrogen Energy*. 29, 635–647 (2004).
[https://doi.org/10.1016/S0360-3199\(03\)00220-9](https://doi.org/10.1016/S0360-3199(03)00220-9)

17. Zhuo, Y., Jung, S., Shen, Y.: Numerical Study of Hydrogen Desorption in an Innovative Metal Hydride Hydrogen Storage Tank. *Energy and Fuels*. 35, 10908–10917 (2021). <https://doi.org/10.1021/acs.energyfuels.1c00666>
18. Ram Gopal, M., Srinivasa Murthy, S.: Copy-right @ International Association for Hydrogen Energy Elsevier Science Ltd STUDIES ON HEAT AND MASS TRANSFER IN METAL HYDRIDE BEDS. (1995)
19. Muthukumar, P., Prakash Maiya, M., Murthy, S.S.: Parametric studies on a metal hydride based single stage hydrogen compressor. (2002)
20. Muthukumar, P., Maiya, M.P., Murthy, S.S.: Experiments on a metal hydride-based hydrogen storage device. *Int J Hydrogen Energy*. 30, 1569–1581 (2005). <https://doi.org/10.1016/j.ijhydene.2004.12.007>
21. Kumar, A., Raju, N.N., Muthukumar, P., Selvan, P.V.: Experimental studies on industrial scale metal hydride based hydrogen storage system with embedded cooling tubes. *Int J Hydrogen Energy*. 44, 13549–13560 (2019). <https://doi.org/10.1016/j.ijhydene.2019.03.180>
22. Raju, N.N., Kumar, A., Malleswararao, K., Muthukumar, P.: Parametric studies on LaNi_{4.7}Al_{0.3} based hydrogen storage reactor with embedded cooling tubes. In: *Energy Procedia*. pp. 2384–2390. Elsevier Ltd (2019)
23. Meng, X., Wu, Z., Bao, Z., Yang, F., Zhang, Z.: Performance simulation and experimental confirmation of a mini-channel metal hydrides reactor. *Int J Hydrogen Energy*. 38, 15242–15253 (2013). <https://doi.org/10.1016/j.ijhydene.2013.09.056>

24. Anbarasu, S., Muthukumar, P., Mishra, S.C.: Tests on $\text{LaNi}_{4.91}\text{Sn}_{0.15}$ based solid state hydrogen storage device with embedded cooling tubes - Part A: Absorption process. *Int J Hydrogen Energy*. 39, 3342–3351 (2014).
<https://doi.org/10.1016/j.ijhydene.2013.12.090>
25. Muthukumar, P., Singhal, A., Bansal, G.K.: Thermal modeling and performance analysis of industrial-scale metal hydride based hydrogen storage container. *Int J Hydrogen Energy*. 37, 14351–14364 (2012).
<https://doi.org/10.1016/j.ijhydene.2012.07.010>
26. Anbarasu, S., Muthukumar, P., Mishra, S.C.: Thermal modeling of $\text{LaNi}_{4.91}\text{Sn}_{0.15}$ based solid state hydrogen storage device with embedded cooling tubes. *Int J Hydrogen Energy*. 39, 15549–15562 (2014).
<https://doi.org/10.1016/j.ijhydene.2014.07.088>
27. Bhouri, M., Goyette, J., Hardy, B.J., Anton, D.L.: Honeycomb metallic structure for improving heat exchange in hydrogen storage system. *Int J Hydrogen Energy*. 36, 6723–6738 (2011). <https://doi.org/10.1016/j.ijhydene.2011.02.092>
28. Bhouri, M., Bürger, I., Linder, M.: Numerical investigation of hydrogen charging performance for a combination reactor with embedded metal hydride and coolant tubes. *Int J Hydrogen Energy*. 40, 6626–6638 (2015).
<https://doi.org/10.1016/j.ijhydene.2015.03.060>
29. Boukhari, A., Bessaïh, R.: Numerical heat and mass transfer investigation of hydrogen absorption in an annulus-disc reactor. *Int J Hydrogen Energy*. 40, 13708–13717 (2015). <https://doi.org/10.1016/j.ijhydene.2015.05.123>

30. Krokos, C.A., Nikolic, D., Kikkinides, E.S., Georgiadis, M.C., Stubos, A.K.: Modeling and optimization of multi-tubular metal hydride beds for efficient hydrogen storage. *Int J Hydrogen Energy*. 34, 9128–9140 (2009). <https://doi.org/10.1016/j.ijhydene.2009.09.021>
31. Singh, A., Maiya, M.P., Srinivasa Murthy, S.: Experiments on solid state hydrogen storage device with a finned tube heat exchanger. *Int J Hydrogen Energy*. 42, 15226–15235 (2017). <https://doi.org/10.1016/j.ijhydene.2017.05.002>
32. Singh, A., Prakash Maiya, M., Srinivasa Murthy, S.: Performance of a solid state hydrogen storage device with finned tube heat exchanger. *Int J Hydrogen Energy*. 42, 26855–26871 (2017). <https://doi.org/10.1016/j.ijhydene.2017.06.071>
33. Mahmoodi, F., Rahimi, R.: Experimental and numerical investigating a new configured thermal coupling between metal hydride tank and PEM fuel cell using heat pipes. *Appl Therm Eng*. 178, (2020). <https://doi.org/10.1016/j.applthermaleng.2020.115490>
34. Bai, X.S., Yang, W.W., Zhang, W.Y., Yang, F.S., Tang, X.Y.: Hydrogen absorption performance of a novel cylindrical MH reactor with combined loop-type finned tube and cooling jacket heat exchanger. *Int J Hydrogen Energy*. 45, 28100–28115 (2020). <https://doi.org/10.1016/j.ijhydene.2020.04.209>
35. Eisapour, A.H., Naghizadeh, A., Eisapour, M., Talebizadehsardari, P.: Optimal design of a metal hydride hydrogen storage bed using a helical coil heat exchanger along with a central return tube during the absorption process. *Int J Hydrogen Energy*. 46, 14478–14493 (2021). <https://doi.org/10.1016/j.ijhydene.2021.01.170>

36. Feng, P., Liu, Y., Ayub, I., Wu, Z., Yang, F., Zhang, Z.: Optimal design methodology of metal hydride reactors for thermochemical heat storage. *Energy Convers Manag.* 174, 239–247 (2018). <https://doi.org/10.1016/j.enconman.2018.08.043>
37. Tong, L., Xiao, J., Yang, T., Bénard, P., Chahine, R.: Complete and reduced models for metal hydride reactor with coiled-tube heat exchanger. *Int J Hydrogen Energy.* 15907–15916 (2019). <https://doi.org/10.1016/j.ijhydene.2018.07.102>
38. Dhaou, H., Souahlia, A., Mellouli, S., Askri, F., Jemni, A., Ben Nasrallah, S.: Experimental study of a metal hydride vessel based on a finned spiral heat exchanger. *Int J Hydrogen Energy.* 35, 1674–1680 (2010). <https://doi.org/10.1016/j.ijhydene.2009.11.094>
39. Mellouli, S., Askri, F., Dhaou, H., Jemni, A., Ben Nasrallah, S.: Numerical simulation of heat and mass transfer in metal hydride hydrogen storage tanks for fuel cell vehicles. *Int J Hydrogen Energy.* 35, 1693–1705 (2010). <https://doi.org/10.1016/j.ijhydene.2009.12.052>
40. Karagiorgis, G., Christodoulou, C.N., von Storch, H., Tzamalís, G., Deligiannis, K., Hadjipetrou, D., Odysseos, M., Roeb, M., Sattler, C.: Design, development, construction and operation of a novel metal hydride compressor. *Int J Hydrogen Energy.* 42, 12364–12374 (2017). <https://doi.org/10.1016/j.ijhydene.2017.03.195>
41. Souahlia, A., Dhaou, H., Askri, F., Sofiene, M., Jemni, A., Ben Nasrallah, S.: Experimental and comparative study of metal hydride hydrogen tanks. *Int J Hydrogen Energy.* 36, 12918–12922 (2011). <https://doi.org/10.1016/j.ijhydene.2011.07.022>

42. Mellouli, S., Askri, F., Dhaou, H., Jemni, A., Nasrallah, S. Ben: A novel design of a heat exchanger for a metal-hydrogen reactor. In: *International Journal of Hydrogen Energy*. pp. 3501–3507. Elsevier Ltd (2007)
43. Wu, Z., Yang, F., Zhang, Z., Bao, Z.: Magnesium based metal hydride reactor incorporating helical coil heat exchanger: Simulation study and optimal design. *Appl Energy*. 130, 712–722 (2014).
<https://doi.org/10.1016/j.apenergy.2013.12.071>
44. Li, H., Wang, Y., He, C., Chen, X., Zhang, Q., Zheng, L., Yang, F., Zhang, Z.: Design and performance simulation of the spiral mini-channel reactor during H₂ absorption. *Int J Hydrogen Energy*. 40, 13490–13505 (2015).
<https://doi.org/10.1016/j.ijhydene.2015.08.066>
45. Wang, H., Prasad, A.K., Advani, S.G.: Hydrogen storage system based on hydride materials incorporating a helical-coil heat exchanger. *Int J Hydrogen Energy*. 37, 14292–14299 (2012). <https://doi.org/10.1016/j.ijhydene.2012.07.016>
46. Wang, D., Wang, Y., Huang, Z., Yang, F., Wu, Z., Zheng, L., Wu, L., Zhang, Z.: Design optimization and sensitivity analysis of the radiation mini-channel metal hydride reactor. *Energy*. 173, 443–456 (2019).
<https://doi.org/10.1016/j.energy.2019.02.033>
47. Askri, F., Ben Salah, M., Jemni, A., Ben Nasrallah, S.: Optimization of hydrogen storage in metal-hydride tanks. *Int J Hydrogen Energy*. 34, 897–905 (2009).
<https://doi.org/10.1016/j.ijhydene.2008.11.021>
48. Garrison, S.L., Hardy, B.J., Gorbounov, M.B., Tamburello, D.A., Corgnale, C., Vanhassel, B.A., Mosher, D.A., Anton, D.L.: Optimization of internal heat

- exchangers for hydrogen storage tanks utilizing metal hydrides. In: International Journal of Hydrogen Energy. pp. 2850–2861 (2012)
49. Andreasen, G., Melnichuk, M., Ramos, S., Corso, H.L., Visintin, A., Triaca, W.E., Peretti, H.A.: Hydrogen desorption from a hydride container under different heat exchange conditions. *Int J Hydrogen Energy*. 38, 13352–13359 (2013). <https://doi.org/10.1016/j.ijhydene.2013.07.115>
50. Bai, X.S., Yang, W.W., Tang, X.Y., Yang, F.S., Jiao, Y.H., Yang, Y.: Optimization of tree-shaped fin structures towards enhanced absorption performance of metal hydride hydrogen storage device: A numerical study. *Energy*. 220, (2021). <https://doi.org/10.1016/j.energy.2020.119738>
51. Chandra, S., Sharma, P., Muthukumar, P., Tatiparti, S.S. V.: Modeling and numerical simulation of a 5 kg LaNi₅-based hydrogen storage reactor with internal conical fins. *Int J Hydrogen Energy*. 45, 8794–8809 (2020). <https://doi.org/10.1016/j.ijhydene.2020.01.115>
52. Raju, M., Kumar, S.: Optimization of heat exchanger designs in metal hydride based hydrogen storage systems. In: International Journal of Hydrogen Energy. pp. 2767–2778 (2012)
53. Visaria, M., Mudawar, I., Pourpoint, T.: Enhanced heat exchanger design for hydrogen storage using high-pressure metal hydride: Part 1. Design methodology and computational results. *Int J Heat Mass Transf*. 54, 413–423 (2011). <https://doi.org/10.1016/j.ijheatmasstransfer.2010.09.029>

54. Kaplan, Y.: Effect of design parameters on enhancement of hydrogen charging in metal hydride reactors. *Int J Hydrogen Energy*. 34, 2288–2294 (2009).
<https://doi.org/10.1016/j.ijhydene.2008.12.096>
55. Nyamsi, S.N., Yang, F., Zhang, Z.: An optimization study on the finned tube heat exchanger used in hydride hydrogen storage system - Analytical method and numerical simulation. *Int J Hydrogen Energy*. 37, 16078–16092 (2012).
<https://doi.org/10.1016/j.ijhydene.2012.08.074>
56. Singh, R., Chakma, S., Birke, V.: Numerical modelling and performance evaluation of multi-permeable reactive barrier system for aquifer remediation susceptible to chloride contamination. *Groundw Sustain Dev*. 10, (2020).
<https://doi.org/10.1016/j.gsd.2019.100317>
57. Chandra, S., Sharma, P., Muthukumar, P., Tatiparti, S.S. V.: Strategies for scaling-up LaNi₅-based hydrogen storage system with internal conical fins and cooling tubes. *Int J Hydrogen Energy*. 46, 19031–19045 (2021).
<https://doi.org/10.1016/j.ijhydene.2021.03.056>
58. Raju, M., Kumar, S.: System simulation modeling and heat transfer in sodium alanate based hydrogen storage systems. *Int J Hydrogen Energy*. 36, 1578–1591 (2011). <https://doi.org/10.1016/j.ijhydene.2010.10.100>
59. Keshari, V., Maiya, M.P.: Design and investigation of hydriding alloy based hydrogen storage reactor integrated with a pin fin tube heat exchanger. *Int J Hydrogen Energy*. 43, 7081–7095 (2018).
<https://doi.org/10.1016/j.ijhydene.2018.02.100>

60. George, M., Mohan, G.: Constructal design of weight optimized metal hydride storage device embedded with ribbed honeycomb. *Appl Therm Eng.* 219, (2023). <https://doi.org/10.1016/j.applthermaleng.2022.119368>
61. Afzal, M., Sharma, P.: Design and computational analysis of a metal hydride hydrogen storage system with hexagonal honeycomb based heat transfer enhancements-part A. *Int J Hydrogen Energy.* 46, 13116–13130 (2021). <https://doi.org/10.1016/j.ijhydene.2021.01.135>
62. Mellouli, S., Dhaou, H., Askri, F., Jemni, A., Ben Nasrallah, S.: Hydrogen storage in metal hydride tanks equipped with metal foam heat exchanger. *Int J Hydrogen Energy.* 34, 9393–9401 (2009). <https://doi.org/10.1016/j.ijhydene.2009.09.043>
63. Laurencelle, F., Goyette, J.: Simulation of heat transfer in a metal hydride reactor with aluminium foam. *Int J Hydrogen Energy.* 32, 2957–2964 (2007). <https://doi.org/10.1016/j.ijhydene.2006.12.007>
64. Ferekh, S., Gwak, G., Kyoung, S., Kang, H.G., Chang, M.H., Yun, S.H., Oh, Y.H., Kim, W., Kim, D., Hong, T., Ju, H.: Numerical comparison of heat-fin-and metal-foam-based hydrogen storage beds during hydrogen charging process. In: *International Journal of Hydrogen Energy.* pp. 14540–14550. Elsevier Ltd (2015)
65. Afzal, M., Sharma, P.: Design of a large-scale metal hydride based hydrogen storage reactor: Simulation and heat transfer optimization. *Int J Hydrogen Energy.* 43, 13356–13372 (2018). <https://doi.org/10.1016/j.ijhydene.2018.05.084>
66. Wang, H., Prasad, A.K., Advani, S.G.: Hydrogen storage systems based on hydride materials with enhanced thermal conductivity. *Int J Hydrogen Energy.* 37, 290–298 (2012). <https://doi.org/10.1016/j.ijhydene.2011.04.096>

67. Minko, K.B., Artemov, V.I., Yan’Kov, G.G.: Numerical study of hydrogen purification using metal hydride reactor with aluminium foam. *Appl Therm Eng.* 76, 175–184 (2015). <https://doi.org/10.1016/j.applthermaleng.2014.11.018>
68. Cui, Y., Zeng, X., Xiao, J., Kou, H.: The comprehensive review for development of heat exchanger configuration design in metal hydride bed, (2022)
69. Sreeraj, R., Aadhithiyan, A.K., Anbarasu, S.: Integration of thermal augmentation methods in hydride beds for metal hydride based hydrogen storage systems: Review and recommendation, (2022)
70. Mellouli, S., Abhilash, E., Askri, F., Ben Nasrallah, S.: Integration of thermal energy storage unit in a metal hydride hydrogen storage tank. *Appl Therm Eng.* 102, 1185–1196 (2016). <https://doi.org/10.1016/j.applthermaleng.2016.03.116>
71. Mellouli, S., Ben Khedher, N., Askri, F., Jemni, A., Ben Nasrallah, S.: Numerical analysis of metal hydride tank with phase change material. *Appl Therm Eng.* 90, 674–682 (2015). <https://doi.org/10.1016/j.applthermaleng.2015.07.022>
72. Ben Mâad, H., Askri, F., Virgone, J., Ben Nasrallah, S.: Numerical study of high temperature metal-hydrogen reactor ($\text{Mg}_2\text{Ni-H}_2$) with heat reaction recovery using phase-change material during desorption. *Appl Therm Eng.* 140, 225–234 (2018). <https://doi.org/10.1016/j.applthermaleng.2018.05.009>
73. El Mghari, H., Huot, J., Xiao, J.: Analysis of hydrogen storage performance of metal hydride reactor with phase change materials. *Int J Hydrogen Energy.* 44, 28893–28908 (2019). <https://doi.org/10.1016/j.ijhydene.2019.09.090>

74. El Mghari, H., Huot, J., Tong, L., Xiao, J.: Selection of phase change materials, metal foams and geometries for improving metal hydride performance. *Int J Hydrogen Energy*. 45, 14922–14939 (2020). <https://doi.org/10.1016/j.ijhydene.2020.03.226>
75. Rabienataj Darzi, A.A., Hassanzadeh Afrouzi, H., Moshfegh, A., Farhadi, M.: Absorption and desorption of hydrogen in long metal hydride tank equipped with phase change material jacket. *Int J Hydrogen Energy*. 41, 9595–9610 (2016). <https://doi.org/10.1016/j.ijhydene.2016.04.051>
76. Niyas, H., Muthukumar, P.: Performance Analysis of Latent Heat Storage Systems. *Int J Sci Eng Res*. 4, (2013)
77. Tong, L., Xiao, J., Bénard, P., Chahine, R.: Thermal management of metal hydride hydrogen storage reservoir using phase change materials. *Int J Hydrogen Energy*. 44, 21055–21066 (2019). <https://doi.org/10.1016/j.ijhydene.2019.03.127>
78. Nyamsi, S.N., Tolj, I., Gęca, M.J.: Dehydrogenation of Metal Hydride Reactor-Phase Change Materials Coupled with Light-Duty Fuel Cell Vehicles. *Energies (Basel)*. 15, (2022). <https://doi.org/10.3390/en15092982>
79. Ye, Y., Lu, J., Ding, J., Wang, W., Yan, J.: Performance improvement of metal hydride hydrogen storage tanks by using phase change materials. *Appl Energy*. 320, (2022). <https://doi.org/10.1016/j.apenergy.2022.119290>
80. Yao, J., Zhu, P., Guo, L., Duan, L., Zhang, Z., Kurko, S., Wu, Z.: A continuous hydrogen absorption/desorption model for metal hydride reactor coupled with PCM as heat management and its application in the fuel cell power system. *Int J*

Hydrogen Energy. 45, 28087–28099 (2020).
<https://doi.org/10.1016/j.ijhydene.2020.05.089>

81. Ye, Y., Lu, J., Ding, J., Wang, W., Yan, J.: Numerical simulation on the storage performance of a phase change materials based metal hydride hydrogen storage tank. *Appl Energy*. 278, (2020). <https://doi.org/10.1016/j.apenergy.2020.115682>
82. Alqahtani, T., Mellouli, S., Bamasag, A., Askri, F., Phelan, P.E.: Thermal performance analysis of a metal hydride reactor encircled by a phase change material sandwich bed. *Int J Hydrogen Energy*. 45, 23076–23092 (2020).
<https://doi.org/10.1016/j.ijhydene.2020.06.126>
83. Alqahtani, T., Bamasag, A., Mellouli, S., Askri, F., Phelan, P.E.: Cyclic behaviors of a novel design of a metal hydride reactor encircled by cascaded phase change materials. *Int J Hydrogen Energy*. 45, 32285–32297 (2020).
<https://doi.org/10.1016/j.ijhydene.2020.08.280>
84. Hassan, I.A., Mohammed, R.H., Ramadan, H.S., Saleh, M.A., Cuevas, F., Hissel, D.: Performance evaluation of a novel concentric metal hydride reactor assisted with phase change material. *Appl Therm Eng*. 224, (2023).
<https://doi.org/10.1016/j.applthermaleng.2023.120065>
85. Mellouli, S., Askri, F., Abhilash, E., Ben Nasrallah, S.: Impact of using a heat transfer fluid pipe in a metal hydride-phase change material tank. *Appl Therm Eng*. 113, 554–565 (2017). <https://doi.org/10.1016/j.applthermaleng.2016.11.065>
86. Ardahaie, S.S., Hosseini, M.J., Eisapour, M., Eisapour, A.H., Ranjbar, A.A.: A novel porous metal hydride tank for hydrogen energy storage and consumption

- assisted by PCM jackets and spiral tubes. *J Clean Prod.* 311, (2021).
<https://doi.org/10.1016/j.jclepro.2021.127674>
87. Bouzgarrou, F., Mellouli, S., Alqahtani, T., Algarni, S.: Parametric study of a metal hydride reactor with phase change materials and heat pipes. *Int J Energy Res.* 46, 4588–4598 (2022). <https://doi.org/10.1002/er.7451>
 88. Tatsidjodoung, P., Le Pierrès, N., Luo, L.: A review of potential materials for thermal energy storage in building applications, (2013)
 89. Drawer, C., Lange, J., Kaltschmitt, M.: Metal hydrides for hydrogen storage – Identification and evaluation of stationary and transportation applications, (2024)
 90. Ben Mâad, H., Askri, F., Ben Nasrallah, S.: Heat and mass transfer in a metal hydrogen reactor equipped with a phase-change heat-exchanger. *International Journal of Thermal Sciences.* 99, 271–278 (2016).
<https://doi.org/10.1016/j.ijthermalsci.2015.09.003>
 91. Nam, J., Ko, J., Ju, H.: Three-dimensional modeling and simulation of hydrogen absorption in metal hydride hydrogen storage vessels, (2012)
 92. Kyoung, S., Ferekh, S., Gwak, G., Jo, A., Ju, H.: Three-dimensional modeling and simulation of hydrogen desorption in metal hydride hydrogen storage vessels. In: *International Journal of Hydrogen Energy.* pp. 14322–14330. Elsevier Ltd (2015)
 93. Shamberger, P.J., Reid, T.: Thermophysical properties of lithium nitrate trihydrate from (253 to 353) K. *J Chem Eng Data.* 57, 1404–1411 (2012).
<https://doi.org/10.1021/jc3000469>

94. Air quality monitoring in NSW: From long term trend monitoring to integrated urban services.
95. Askri, F., Jemni, A., Nasrallah, S. Ben: Study of two-dimensional and dynamic heat and mass transfer in a metal-hydrogen reactor. (2003)
96. Wu, W., Sung, F., Chuu, S.: Thermal conductivity of polyurethane foams.
97. Jiang, T., Gradus, J.L., Rosellini, A.J.: Supervised Machine Learning: A Brief Primer. (2020)
98. Masson, J.F., Biggins, J.S., Ringe, E.: Machine learning for nanoplasmonics, (2023)
99. Ozbas, E.E., Aksu, D., Ongen, A., Aydin, M.A., Ozcan, H.K.: Hydrogen production via biomass gasification, and modeling by supervised machine learning algorithms. Int J Hydrogen Energy. 44, 17260–17268 (2019). <https://doi.org/10.1016/j.ijhydene.2019.02.108>
100. Matsuo, Y., LeCun, Y., Sahani, M., Precup, D., Silver, D., Sugiyama, M., Uchibe, E., Morimoto, J.: Deep learning, reinforcement learning, and world models. Neural Networks. 152, 267–275 (2022). <https://doi.org/10.1016/j.neunet.2022.03.037>
101. Yu, X., Shen, Y., Guan, Z., Zhang, D., Tang, Z., Li, W.: Multi-objective optimization of ANN-based PSA model for hydrogen purification from steam-methane reforming gas. Int J Hydrogen Energy. 46, 11740–11755 (2021). <https://doi.org/10.1016/j.ijhydene.2021.01.107>
102. Vo, N.D., Kang, J.H., Oh, D.H., Jung, M.Y., Chung, K., Lee, C.H.: Sensitivity analysis and artificial neural network-based optimization for low-carbon H₂ production via a sorption-enhanced steam methane reforming (SESMR) process

- integrated with separation process. *Int J Hydrogen Energy*. 47, 820–847 (2022).
<https://doi.org/10.1016/j.ijhydene.2021.10.053>
103. Sun, K., Esnaola, I., Okorie, O., Charnley, F., Moreno, M., Tiwari, A.: Data-driven modeling and monitoring of fuel cell performance. *Int J Hydrogen Energy*. 46, 33206–33217 (2021). <https://doi.org/10.1016/j.ijhydene.2021.05.210>
 104. Guarino, A., Spagnuolo, G.: Automatic features extraction of faults in PEM fuel cells by a siamese artificial neural network. *Int J Hydrogen Energy*. 46, 34854–34866 (2021). <https://doi.org/10.1016/j.ijhydene.2021.08.024>
 105. Rahnama, A., Zepon, G., Sridhar, S.: Machine learning based prediction of metal hydrides for hydrogen storage, part I: Prediction of hydrogen weight percent. *Int J Hydrogen Energy*. 44, 7337–7344 (2019).
<https://doi.org/10.1016/j.ijhydene.2019.01.261>
 106. Rahnama, A., Zepon, G., Sridhar, S.: Machine learning based prediction of metal hydrides for hydrogen storage, part II: Prediction of material class. *Int J Hydrogen Energy*. 44, 7345–7353 (2019). <https://doi.org/10.1016/j.ijhydene.2019.01.264>
 107. Wang, C.S., Brinkerhoff, J.: Predicting hydrogen adsorption and desorption rates in cylindrical metal hydride beds: Empirical correlations and machine learning. *Int J Hydrogen Energy*. 46, 24256–24270 (2021).
<https://doi.org/10.1016/j.ijhydene.2021.05.007>
 108. Suwarno, S., Dicky, G., Suyuthi, A., Effendi, M., Witantyo, W., Noerochim, L., Ismail, M.: Machine learning analysis of alloying element effects on hydrogen storage properties of AB₂ metal hydrides. *Int J Hydrogen Energy*. 47, 11938–11947 (2022). <https://doi.org/10.1016/j.ijhydene.2022.01.210>

109. Nations, S., Nandi, T., Ramazani, A., Wang, S., Duan, Y.: Metal hydride composition-derived parameters as machine learning features for material design and H₂ storage. *J Energy Storage*. 70, (2023). <https://doi.org/10.1016/j.est.2023.107980>
110. Batalović, K., Radaković, J., Kuzmanović, B., Medić Ilić, M., Paskaš Mamula, B.: Machine learning-based high-throughput screening of Mg-containing alloys for hydrogen storage and energy conversion applications. *J Energy Storage*. 68, (2023). <https://doi.org/10.1016/j.est.2023.107720>
111. Tiwari, S., Gupta, N., Kumar, S., Kumar, A., Sharma, P.: Experimental investigation, development of machine learning model and optimization studies of a metal hydride reactor with embedded helical cooling tube. *J Energy Storage*. 72, (2023). <https://doi.org/10.1016/j.est.2023.108522>
112. Verma, A., Wilson, N., Joshi, K.: Solid state hydrogen storage: Decoding the path through machine learning. *Int J Hydrogen Energy*. 50, 1518–1528 (2024). <https://doi.org/10.1016/j.ijhydene.2023.10.056>
113. Kumar, A., Tiwari, S., Gupta, N., Sharma, P.: Machine learning modelling and optimization for metal hydride hydrogen storage systems. *Sustain Energy Fuels*. 8, 2073–2086 (2024). <https://doi.org/10.1039/d4se00031e>
114. Kanti, P.K., Shrivastav, A.P., Sharma, P., Maiya, M.P.: Thermal performance enhancement of metal hydride reactor for hydrogen storage with graphene oxide nanofluid: Model prediction with machine learning. *Int J Hydrogen Energy*. 52, 470–484 (2024). <https://doi.org/10.1016/j.ijhydene.2023.03.361>

115. Maulud, D., Abdulazeez, A.M.: A Review on Linear Regression Comprehensive in Machine Learning. *Journal of Applied Science and Technology Trends*. 1, 140–147 (2020). <https://doi.org/10.38094/jastt1457>
116. An, S., Liu, W., Venkatesh, S.: Face Recognition Using Kernel Ridge Regression.
117. Rajeswari, R., Satheesh Kumar, J., Devi, T., Bharathiar University. Department of Computer Applications, Institute of Electrical and Electronics Engineers: LASSO: A Feature Selection Technique In Predictive Modeling For Machine Learning.
118. Awad, M., Khanna, R.: Efficient Learning Machines. https://doi.org/https://doi.org/10.1007/978-1-4302-5990-9_4
119. Basak, D., Pal, S., Patranabis, D.C.: Support Vector Regression. (2007)
120. Xu, M., Watanachaturaporn, P., Varshney, P.K., Arora, M.K.: Decision tree regression for soft classification of remote sensing data. *Remote Sens Environ*. 97, 322–336 (2005). <https://doi.org/10.1016/j.rse.2005.05.008>
121. Bentéjac, C., Csörgő, A., Martínez-Muñoz, G.: A comparative analysis of gradient boosting algorithms. *Artif Intell Rev*. 54, 1937–1967 (2021). <https://doi.org/10.1007/s10462-020-09896-5>
122. Agatonovic-Kustrin, S., Beresford, R.: Basic concepts of artificial neural network (ANN) modeling and its application in pharmaceutical research. (2000)
123. Srirekha, A., Bashetty, K.: Infinite to finite: An overview of finite element analysis, (2010)